Massimino et al. *Microsystems & Nanoengineering* (2026)12:248
https://doi.org/10.1038/s41378-026-01256-7

Microsystems & Nanoengineering
www.nature.com/micronano

ARTICLE Open Access

Fully flexible large-area MEMS-based triaxial force sensor compatible with flat panel display manufacturing

Gianluca Massimino[1]✉, Samer Houri[1], Alexey Podkovskiy[1], Veronique Rochus[1] and Jan Genoe[1]

Abstract

This work describes a fully flexible capacitive Micro-Electro-Mechanical-Systems (MEMS) based Large-Area (LA) triaxial force sensor, compatible with the Flat Panel Display (FPD) production. Thus, it is obtained by means of standard surface micromachining, unlike the reported other flexible sensor technologies, which are based on ad-hoc fabrication processes, that limit their large-scale manufacturing, area covering feature and flexibility. The triaxial force sensor is referred to as pixel. Its response is characterized in the mechanical and electrical domains. The effects of the fabrication-induced residual stresses as well as the applied external pressure and shear load are measured. The 3D Finite Element Method (FEM) model correctly captures the initial deflection due to the residual stresses. It properly simulates the pressure and shear behavior taking into account the contact between the embedded MEMS and the substrate. It represents a valuable tool to provide design guidelines for the MEMS optimization. The pixel normalized pressure sensitivity is equal to 0.0013 kPa^{-1}. While the shear one is 2.6×10^{-3} kPa^{-1}. The sensitivity values of the presented device are higher than those reported for state-of-the-art capacitive triaxial force sensors. Potential sensing capability and scalability of the array design are preliminary proved. Referring to a 29×29 array with 1 cm^2 footprint, the predicted initial capacitance of each independent capacitor element is equal to 640 pF. The related pressure and differential shear sensitivities are 0.841 pF/kPa and 2.859 pF/kPa, respectively. The presented work describes a novel technology for highly sensitive flexible triaxial force sensors compatible with LA FPD cost-effective batch production.

Introduction

Nowadays, flexible electronics technology[1] compatible with the Flat Panel Display (FPD) fabrication process is the focus of attention for the production of Thin Film Transistor (TFT) based bendable screens. It provides a cost-effective Large-Area (LA) manufacturing in combination with a flexible form factor. A standard generation 11 FPD fabrication plant currently produces Organic Light-Emitting Diode (OLED) display sheets on substrates with sizes up to 3000×3320 mm^2. The application of a flexible electronics in different research fields is reported in refs. [2–5], however, showing a very limited compatibility with the FPD batch production capability. An innovative use of it is investigated at imec, Leuven (BE) to create flexible LA Micro-Electro-Mechanical-Systems (MEMS) fully compatible with the FPD manufacturing, to sensorize any curved surface[6]. FPD technology overcomes the limits in active surface of Silicon (Si) based technologies, which are characterized by their rigidity and their small area.

Increasingly, fields of application, e.g., automotive, consumer electronics, robotics and prosthetics[7–9] require more sophisticated touch sensing features. Flexible triaxial force sensors[10] are crucial in such markets to enable more intuitive applications, safe human-machine interactions and increase the devices usability[11–13].

Touchscreens that are widely adopted in home appliances, infotainment systems[14], consumer electronics[15,16], smartphones and tablets[17,18] and medical devices[19] require tactile feedback to the user, that mimics the natural detected pressure felt by pressing physical buttons, as one of the main targets of the next generation technology. This required haptic feedback is achieved using Micromachined Ultrasonic Transducers (MUTs) technology[20–24]. Such

Correspondence: Gianluca Massimino (gianluca.massimino@outlook.com)
[1]imec, Kapeldreef 75, 3001 Leuven, Belgium

existing devices adopt either a piezoelectric material active layer[25–28] resulting in Piezoelectric MUTs (PMUTs)[29–33] or they are based on the capacitive transduction principle Capacitive MUTs (CMUTs)[34–37]. Compatibility with the FPD fabrication process is demonstrated for both PMUTs and CMUTs devices, characterized by a fully flexible large area tiling[38–41].

The fields of robotics research and Electronic Skin (E-Skin)[42–45] aim to provide a human skin-like capability to robots, in order to detect sensory tactile stimuli. Robotic devices would benefit from the integration of flexible large-area triaxial force sensors. As such, a goal of this field is to achieve the dexterous object manipulation by intelligent grippers[46–48]. As a matter of fact, the grip and the touch feeling relates to the independent detection of shear and pressure load conditions due to an external force oriented along a direction of the tridimensional space. Equipping medical robots, service robots, collaborative (cobots) and wearable robots (such as prosthetics and exoskeletons) with triaxial force sensors represents a need for the next generation technology[49–52].

Distributed triaxial force sensors enable the creation of human-machine sensorized interfaces for wearable robots with multiple applications. On one hand, the comfort evaluation of the wearer in order to reduce skin injures that are very frequent in people wearing a prosthesis or exoskeletons for aided movements. On the other hand, the intention recognition and prediction of motion, by the correlation of the detected skin shear and pressure stresses to the deep muscle activity, for a natural human-like and real-time musculoskeletal assistance provided by active devices[53–55].

Capacitive triaxial force sensors, that are currently manufactured through standard micromachining processes, are based on monolithic Si-MEMS with embedded CMOS technology. However, they are rigid and they can be either assembled on a rigid-flex printed circuit board (PCB) or integrated on a rigid substrate characterized by a reduced area covering factor and spatial sensitivity. They don't provide enough flexibility to be deployed on curved surfaces for conformal covering. The pressure and shear sensitivities are respectively limited to the order of 10^{-1} pF/kPa and 10^{-2} pF/kPa due to the limits of the fabrication scheme. In fact, the creation of a sensing capacitor is possible by means of the wafer-to-wafer bonding of the Si-MEMS and the CMOS electronics with electrically conductive bond pads and Through-Si-Vias (TSV). However, the smallest fabricated capacitor gap is limited to the order of 1 μm resulting in reduced sensing features[56–61].

In the relevant currently reported literature, flexible capacitive triaxial force sensors, on the other hand, are not compatible with the micromachining batch production. At present, their fabrication is based on ad-hoc complex non-standard processes consisting, for instance, in casting elastomer components into tailored 3D printed molds, 3D printed parts and Layer-By-Layer (LBL) assembly by means of advanced vertical aligning laboratory tools. Therefore, they are characterized by a smallest features size of the order of 1 mm[62,63]. The obtained devices rely on stretchable elastomer materials, which are known to be largely affected by thermal expansion, hygroscopic effects and degradation. In devices of this type, the performance is very sensitive to the deformation induced by the bending of the substrate that limits their stability when applied over a deformable surface. The stability is also affected by the long-term deformation effects related to the viscoelastic creep phenomenon that causes in-time signal drifting when the device is subjected to constant long-term stresses induced by either an external load or a curvature of the substrate during the conformal covering of a curved surface. Moreover, the stretchable behavior of the elastomer doesn't provide a sufficient displacement restrain. Hence, the device performance is limited to a range of application of few 10^1 kPa[64,65] that limits the sensor Full Scale (FS) range.

In the capacitive triaxial force sensors, the application of a normal pressure load over a movable surface of a plate capacitor implies a local out-of-plane displacement along the normal direction. It is associated with the capacitor gap variation and, consequently, the change of capacitance. It represents the related pressure sensing mechanism[66,67]. On the other direction, a shear load condition due to an external in-plane directed force distribution, naturally, translates into a local in-plane translation and a rotation. The rotation is caused by an induced bending moment with respect to the center of rotation of the system, with consequently an out-of-plane displacement distribution. Therefore, the shear sensing mechanism relates to the combination of both in-plane and out-of-plane movements. In this case, the translation implies a decrease of the capacitor electrodes' overlapping area and the latter causes a change of capacitor gap. In other words, the reduction of overlapping area leads to a decrease of capacitance, while the gap variation translates into an increased or a decreased capacitance depending on the variation sign. A gap reduction implies a capacitance increase, on the contrary, a gap increment gives a capacitance decrease. For this reason, shear and pressure sensing mechanisms are not independent and such devices are intrinsically characterized by coupled sensing features. The presence of both effects may either compensate each other or create a situation in which one of the two movements disturbs the generated read-out signal. In certain load conditions no signal is obtained because of the compensation or the excessive disturbance[68,69]. In the monolithic Si-MEMS technology, the described behavior is mitigated by means of in-plane beam-like springs with almost infinite axial stiffness compared to the transversal one. Thus, the in-plane translation is always negligible with respect to the out-of-plane one. On the contrary, in the elastomer based devices the axial and transversal stiffness are comparable and a restrained in-plane translation is not possible.

This paper presents a flexible triaxial force sensor, compatible with standard FPD processing for a LA manufacturing. It consists of an arrangement on a flexible foil, i.e. a patch, of independent micro force sensing devices, referred to as pixels, analogously to pixels in an image sensor, that embed a MEMS-based structure, with independent pressure and shear sensing. Thus, the proposed device represents an innovation with respect to the described literature works. The key novelties and advantages in this work are: (a) the cost-effective batch production, thanks to the FPD fabrication compatibility; (b) the adaptation to any curved deformable surfaces, due to the flexibility of the foil; (c) the definition of different sensor patch sizes, thanks to highly versatile large area tiling; (d) the independency of the MEMS pressure and shear sensing features, that are not affected by parasitic deformation mechanism; (e) the sensor spatial sensitivity of the order of 1 μm thanks to the micromachining based manufacturing; (f) and a highly sensitive performance due to an efficient design.

The novel sensor stack is described and the fabrication results are shown. Moreover, a capacitive electro-mechanical analytical model of the performing behavior is obtained together with a 3-Dimensional (3D) multi-physics numerical simulation strategy. The proposed numerical model takes into account the contact problem between the suspended MEMS and the substrate and the fabrication-induced residual stresses in the different materials. Furthermore, its experimental validation is presented in the mechanical and electrical domain. Hence, the proof-of-concept is shown and assessed by means of measurements and simulations, relating to both the pressure and shear load conditions. Normalized pressure sensitivity is equal to $0.0013\,\text{kPa}^{-1}$. While the shear one results $2.6 \times 10^{-3}\,\text{kPa}^{-1}$. They way more exceed the state-of-the-art capacitive triaxial force sensors' ones. Preliminary array characterization results give an initial validation of the sensing capability and the sensitivity scalability at the array level. They predict that a device with 1 cm^2 footprint area would have a pressure sensitivity of 0.841 pF/kPa, while the differential shear sensitivity is 2.859 pF/kPa.

This manuscript is organized as follows.

In Section "Device", the design of the device is presented. The sensor stack is shown together with the design features and dimensions.

Section "Fabrication" is focused on the results of the fabrication.

Section "3-Dimensional multiphysics model" is devoted to the 3D multiphysics modeling of the device behavior. The 3D Finite Element Method (FEM) model is described with a focus on the FEM domains, boundary conditions and discretization. The carried out analyses and the performance computation strategy are discussed. The working principle is explained by means of an analytical formulation.

Section "Numerical and experimental results" regards the experimental characterization campaign. Performed measurements in the mechanical and electrical domain are presented. Hence, the numerical model experimental validation is shown and the sensor pressure and shear sensitivities are obtained.

The paper concludes in Section "Conclusion".

Device

This section focuses on the design of the flexible LA pressure and shear sensor patch, based on sensing micro pixels with integrated MEMS. In particular, the sensor stack, compatible with the FPD manufacturing and the MEMS sensing features are detailed and the working principle explanation is given.

A portion of the sensor patch is represented in Fig. 1a, where a 3D sketch of the device is presented, including the description of the different components and materials. It consists of an arrangement of micro pixel sensing units (see a detail in Fig. 1b) with triaxial force detection features, fabricated on a flexible Polyimide (PI) foil. The pixel embeds a capacitive MEMS. It consists of a Si_3N_4 butterfly-shaped plate, suspended over four bridges, with an integrated Ti/Pt top electrode. In addition, a photosensitive organic epoxy permanent material, dry film resist (referred to as DFR) is placed on top of the layered plate forming a central bump. The role of this layer is to capture the in-plane forces. Furthermore, the pixel is coated by a photosensitive Siloxane-based elastomer SINR, provided by Shin-Etsu Chemical Co., Ltd, that creates a soft coating where the external load is applied and forms a barrier for the external dust and liquids in order to protect the embedded MEMS.

Plane cuts of the capacitive MEMS-based sensing structure are shown in Fig. 1c, d. For clarity, the protective elastomer is not depicted. The four independent Ti/Pt bottom electrodes form along with the top electrode one that is integrated into the suspended butterfly layered plate, four independent capacitors, namely, C_{11}, C_{12}, C_{21}, C_{22} that are visible in the top view presented in Fig. 1c. Note that the system is characterized by a double symmetry that guarantees the isotropy of the in-plane response.

According to the reported characteristic parameters, the bottom electrode size is $\text{L} = 115\ \mu\text{m}$, the square pixel side length is $l_{pixel} = 300\ \mu\text{m}$, the separation width from the Si_3N_4 lateral wall is $w_{trench} = 10\ \mu\text{m}$, while the connecting ligaments

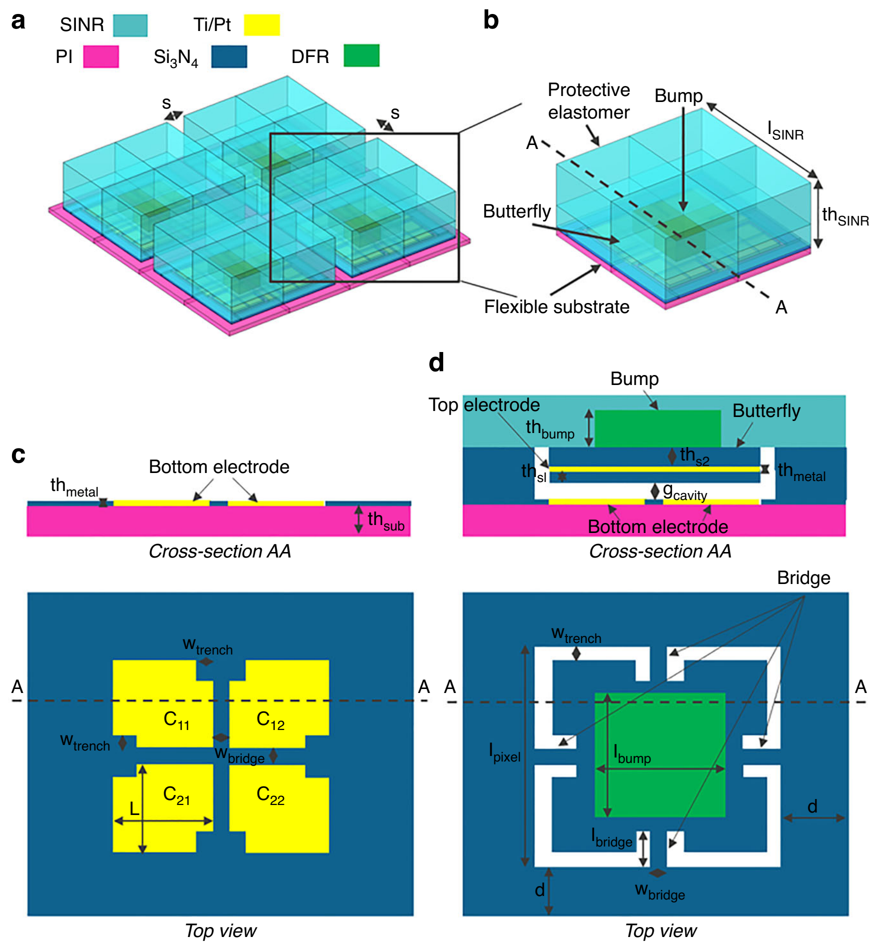

Fig. 1 Sketch of the flexible triaxial force sensor with the description of main components, materials and characteristic dimensional parameters. a A patch portion. **b** Sensing micro pixel. **c** Cross-section AA and top view of the bottom electrodes. **d** Cross-section AA and top view of the embedded MEMS

are characterized by a length $l_{bridge} = 128\,\mu m$ and a width $w_{bridge} = 50\,\mu m$. They are monolithically linked to the Si_3N_4 lateral wall with size $d = 35\,\mu m$. One may notice that the four corners of the butterfly wings are vertically aligned with the capacitors, which are separated by w_{bridge} along the horizontal directions. As reported in the cross-section AA view, the flexible PI substrate has a thickness equal to $th_{sub} = 15\,\mu m$, while, bottom and top electrode metals are two layers stack with a thickness of $th_{metal} = 130\,nm$ where 10 nm refers to the Ti adhesion layer while the remaining 120 nm consists of Pt. The Si_3N_4 structural layer thickness is formed by two conformal depositions with thickness $th_{s1} = 100\,nm$ and $th_{s2} = 2.6\,\mu m$. In particular, the former coating role is to separate the top electrode from the air cavity to prevent any short circuit in case of contact with the bottom electrodes. While the latter coating creates the main structural layer that governs the stiffness and, consequently, the MEMS sensing response. The thin air cavity gap is $g_{cavity} = 90\,nm$, the square bump is centrally placed over the butterfly layered plate and it has a lateral size $l_{bump} = 150\,\mu m$ while the corresponding thickness is $th_{bump} = 50\,\mu m$. The protective SINR elastomer soft coating is photopatterned on the MEMS sensing part. It is centered and square with sides $l_{SINR} = 335\,\mu m$ and a thickness $th_{SINR} = 100\,\mu m$, while the array spacing parameter is $s = 30\,\mu m$.

Fabrication

The device is manufactured in the advanced cleanroom laboratory at imec in Leuven, Belgium. The processing development is carried out on standard 150 mm (6 in) glass wafer with thickness of 500 μm. The goal of this procedure is to speed up the development on handy substrates maintaining the full processing compatibility with the FPD manufacturing.

Fabrication process

The step-by-step description of the fabrication process is provided in Fig. 2. Note that alternative materials and

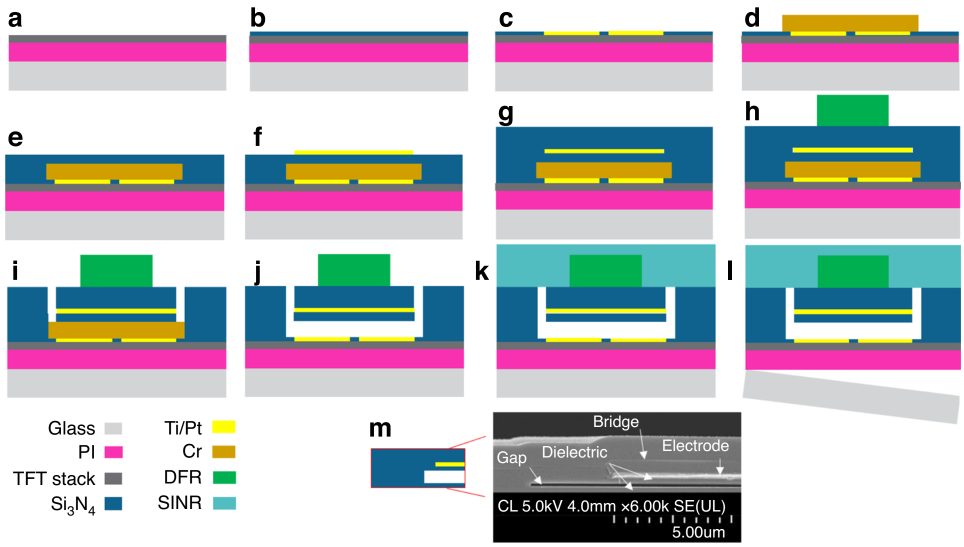

Fig. 2 Fabrication process flow. a TFT stack deposition on a spin-coated PI substrate on a temporary glass carrier. **b** Deposited Si_3N_4 dielectric layer. **c** Patterned bottom electrode. **d** Deposited sacrificial layer. **e** Deposited MEMS Si_3N_4 dielectric layer. **f** Patterned top electrode. **g** Deposited MEMS Si_3N_4 structural layer. **h** Creation of the bump. **i** Trenches to sacrificial layer opening. **j** Sacrificial release. **k** Laminated elastomer coating. **l** Laser lift-off delamination. **m** SEM cross-section of the edge of a bridge-like structure with description of different layers

convectional techniques may be used to create the same cross-section. Hereafter, a description of the key fabrication aspects, reported in the authors' patent[70], is given with particular attention on the creation of the MEMS thin gap, providing alternative methodologies available in literature. As the first step, the flexible substrate U-Varnish-S Polyimide (UBE) is spin-coated on the temporary glass carrier and cured at 450 °C. Then, the compatibility with the FPD manufacturing allows for the deposition of a TFT stack on the PI polymer, to act as the embedded electronics to reach and control each individual pixel[71,72]. It is currently used in TFT-based capacitive fingerprint sensors able to detect 1 fF of capacitance variations[73,74]. Since the MEMS-based sensor is here purely demonstrated, the TFT stack represents only the metal routing without altering the generality of the process flow. Continuing, a Si_3N_4 dielectric layer is deposited by means of Plasma-Enhanced Chemical Vapor Deposition (PECVD). The bottom electrode is then created by means of the self-aligned lift-off processing. It consists in dry etching the Si_3N_4, in correspondence of the metal place, with the aid of a photo-resist mask that is kept as the lift-off layer for the subsequent metal deposition. This technique reduces the step coverage issue in the next steps[75]. The Si_3N_4 etching is performed through Deep Reactive Ion Etching (DRIE) by means of SF_6/O_2 while the Ti/Pt metal is evaporated. The patterned Cr sacrificial layer is deposited through evaporation and covered by a PECVD obtained Si_3N_4 dielectric layer. Note that a dry etched sacrificial release technique, in combination with a Cu sacrificial layer, to create suspended MEMS over thin gaps with good uniformity is already demonstrated in ref. [76], where Si_3N_4-based CMUTs are fabricated by means of a large-area FPD compatible process based on Gen 3.5 glass panels. While a $XeFe_2$ dry etching sacrificial release with a Mo sacrificial layer is used in ref. [77], with high selectivity against Si_3N_4[78]. A $XeFe_2$ - Mo dry sacrificial release technique, for MEMS devices, compatible with FPD manufacturing based on Gen 4.5 glass panels, is also proved in ref. [79], for the fabrication of integrated MEMS-and-TFT-on-Glass. Subsequently, the top electrode is evaporated, patterned and covered by the Si_3N_4 structural layer. This layer is deposited by means of PECVD under controlled conditions in terms of temperature, pressure, RF power and SiH_4 and N_2 gas flows in order to control the residual stress in the layer, as demonstrated in refs. [80,81], where tensile and compressive stresses are obtained at different deposition conditions. Subsequently, an organic epoxy permanent highly cross-linked DFR material is laminated at a temperature of 40 °C and patterned to create the bump. The trenches through the Si_3N_4 to the Cr sacrificial layer are opened by means of SF_6/O_2 dry etching (DRIE). The MEMS is released by means of a wet etching, using Cr etchant (Chromium Etchant 1020, Transene, Danvers, MA, USA). The device is immersed for 4 h to etch away the Cr sacrificial layer. Subsequently, a CO_2-based critical point dryer (Automegasamdri-916B, Tousimis, Rockville, MD, USA) is used to prevent capillary stiction. The created thin gap is visible in Fig. 2m. The elastomer soft coating dry film SINR 3570 is laminated with a lamination pressure of 100 kPa and temperature of 80 °C. It is photo-patterned using I-line

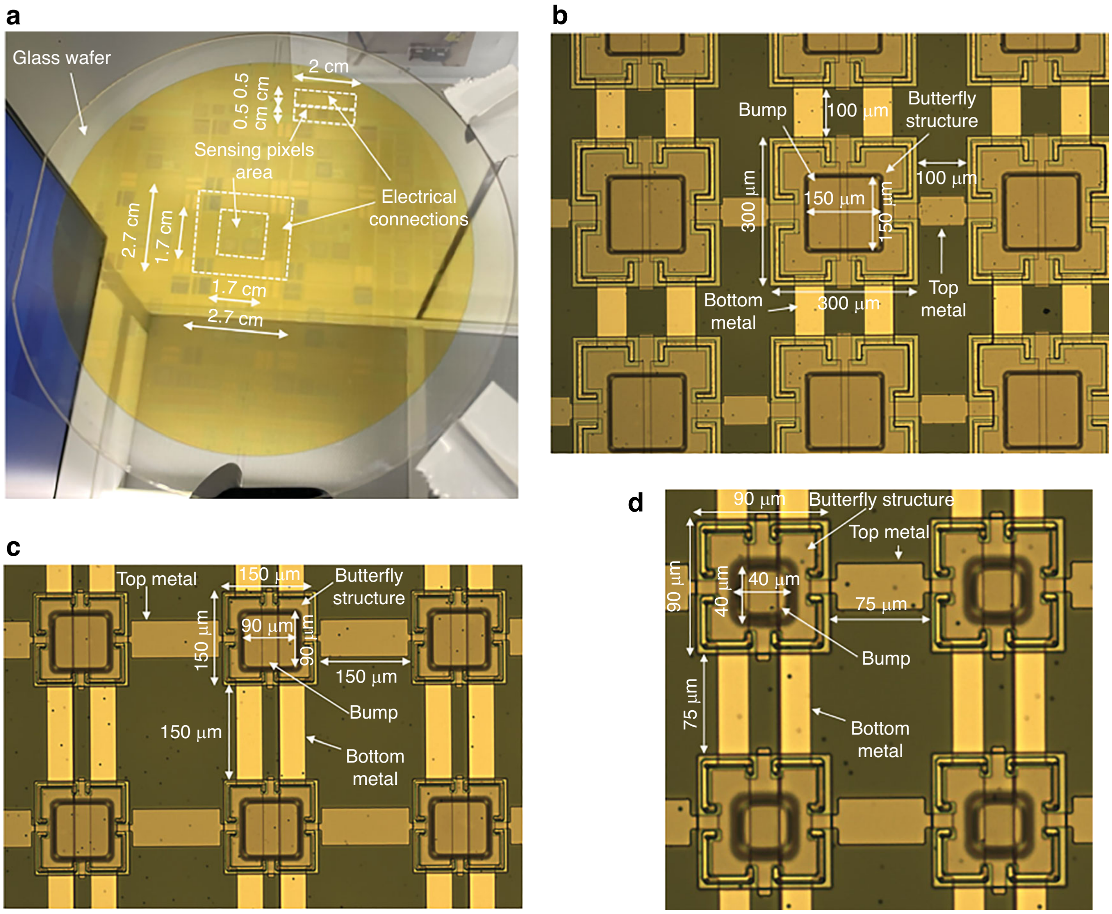

Fig. 3 Full-stack sensor patches with description of the main components and dimensions. a Mapped patches on a 150 mm (6 in) glass wafer. **b** A portion of a fabricated patch with $300 \times 300\ \mu m^2$ butterfly structure size, 100 μm regular spacing and $150 \times 150\ \mu m^2$ central bump size. **c** A portion of a fabricated patch with $150 \times 150\ \mu m^2$ butterfly structure size, 150 μm regular spacing and $90 \times 90\ \mu m^2$ central bump size. **d** A portion of a fabricated patch with $90 \times 90\ \mu m^2$ butterfly structure size, 75 μm regular spacing and $40 \times 40\ \mu m^2$ central bump size

exposure at 2000 mJ/cm^2 and a Post Exposure Bake (PEB) at 110 °C for 2'[82,83]. It has the ability to bridge over features with nearly zero shrinkage after curing[84–86]. Finally, the flexible device is released by Laser Lift-Off (LLO) from the glass carrier.

Fabrication results

Figure 3a shows the sensor patches mapped on a glass wafer, where two patch sizes are highlighted, namely, $2.7 \times 2.7\ cm^2$ and $2 \times 1\ cm^2$. In the two considered cases, the sensing pixels area is respectively equal to $1.7 \times 1.7\ cm^2$ and $2 \times 0.5\ cm^2$, while the remaining patch area is occupied by the electrical connections for further electronics integration. Note that the PI-based stack is almost transparent.

To show the results of the fabrication process steps, a portion of the described sensor patch in the previous section is presented in Fig. 3b. The main components description regarding the top and bottom metals, the sensing layered plate, indicated with "butterfly structure" and central bump are indicated along with the related characteristic dimensions.

Additionally, other pixel sizes are manufactured. Figure 3c shows a fabricated patch portion with 150 μm regular spacing, butterfly layered plate size equal to $150 \times 150\ \mu m^2$ and central bump dimension of $90 \times 90\ \mu m^2$. In Fig. 3d, a portion of a 75 μm regularly spaced arrangement is reported with $90 \times 90\ \mu m^2$ butterfly structures footprint and central bumps size of $40 \times 40\ \mu m^2$.

The sensor patches present a sensing area where pixels are allocated and a peripheral area dedicated to the electrical connections to the outside electronics. They are diced and delaminated from the glass substrate to achieve different patch sizes and a commercially available 68 pins Flexible Printed Circuit (FPC), to act as flexible electrical connector to the downstream electronics, is bonded on the sides, as presented Fig. 4a. Note that, thanks to the

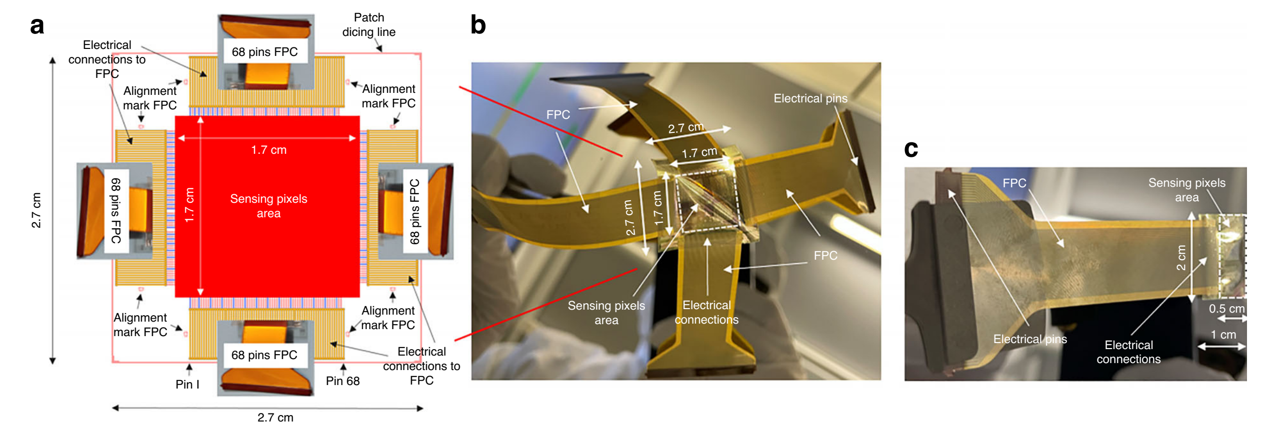

Fig. 4 Fabricated fully flexible sensor patch with description of the main components and dimensions. a Schematic representation of the patch with description of the main components **b** Patch with size 2.7×2.7 cm^2 and four flex electrical connectors. **c** Patch with size 2×1 cm^2 and one flex electrical connector

FPD manufacturing compatibility, standard connections to external electronic components, used in TFT-display technology are possible[87]. The results of this procedure are presented in Fig. 4b, where four flexible (flex) connectors are glued to the four sides of a 2.7×2.7 cm^2 footprint sensor patch, while Fig. 4c shows a 2×1 cm^2 footprint sensor patch with only one flex connector.

The fabrication results demonstrate the versatility of the fabrication process, as well as, the potential of the first pressure and shear sensor with fully flexible features and compatibility with the LA FPD batch production.

3-dimensional multiphysics model

Numerical model

A 3-Dimensional (3D) Finite Element Method (FEM) numerical model is built in COMSOL Multiphysics 5.6. The pixel presented in Section "Device" is modeled considering the full layered stack and the MEMS design features.

The mechanical pixel response is governed by the elasticity equations. In particular, given the incompressibility of the SINR soft coating, the mixed FEM formulation is implemented, in terms of the unknowns (π, $\boldsymbol{u}$), where $\pi(\boldsymbol{x})$ represents the pressure parameter field and $\boldsymbol{u}(\boldsymbol{x})$ the 3D displacement field[88,89]. While in the remaining compressible FEM domains the displacement formulation is adopted.

The fabrication-induced residual stresses are taken into account by means of an amount of initial isotropic stress acting in the plane of each layer. Hence, each material is subjected to a particular uniform membrane stress, depending on the manufacturing process, so that the device layered cross-section is characterized by both tensile and compressive stresses.

It is worth noting that the pixel characteristic dimension is of the order of 100 µm. Therefore, it is very small with respect to a size ≥1 mm.

The device response is computed considering a distribution of external surface load $\boldsymbol{f}(\boldsymbol{x})$ applied to the pixel top surface S_f, as depicted in Fig. 5a and expressed by the condition (1)

$$\boldsymbol{\sigma}(\boldsymbol{x}) \cdot \boldsymbol{n}(\boldsymbol{x}) = \boldsymbol{f}(\boldsymbol{x}) \text{ on } S_f \tag{1}$$

where $\boldsymbol{\sigma}(\boldsymbol{x})$ represents the Cauchy stress tensor and $\boldsymbol{n}(\boldsymbol{x})$ is the outward normal unit vector.

Given this surface of contact between the sensor and an external body with smallest feature ≥1 mm, when they get in touch with each other and a transmission of contact forces occurs over the area. In this case, the applied external load is considered uniformly distributed over the surface.

Displacement conditions are enforced, as reported in the Eqs. (2) and (3),

$$\boldsymbol{u}(\boldsymbol{x}) = \boldsymbol{0} \text{ on } S_{bot} \tag{2}$$

$$\boldsymbol{u}(\boldsymbol{x}) \cdot \boldsymbol{n}(\boldsymbol{x}) = 0 \text{ on } S_{lat} \tag{3}$$

where S_{bot} represents the bottom surface of substrate, S_{lat} is the lateral surface of the substrate and $\boldsymbol{n}(\boldsymbol{x})$ is the outward normal unit vector.

Note that the condition (2) implies that the substrate is clamped without any movements, while Eq. (3) corresponds to a lateral displacement restrain due to the symmetry of the system.

The embedded MEMS sensing structure is suspended over a thin cavity with thickness equal to g_{cavity}, therefore, a contact reaction is obtained when the following contact condition between the butterfly structure bottom surface

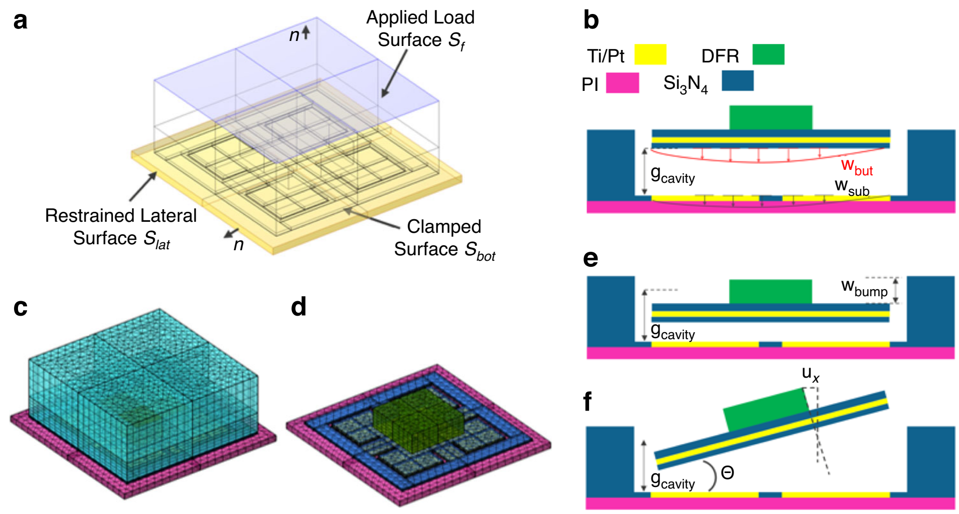

Fig. 5 Sensing pixel model description. a Applied load surface S_f in blue and displacement boundary conditions surfaces S_{lat} and S_{bot} in yellow. **b** Embedded MEMS cross-section AA with highlighted initial cavity gap g_{cavity}, substrate top surface vertical displacement w_{sub} and butterfly bottom surface vertical displacement w_{but}. **c** Pixel 3D FEM discretization transparent view **d** Detail of the embedded MEMS 3D FEM discretization transparent view. **e** Pressure sensing mechanism: cross-section AA schematic representation with exaggerated motion of the embedded MEMS. **f** Shear sensing mechanism: cross-section AA schematic representation with exaggerated motion of the embedded MEMS

and the flexible substrate top surface occurs

$$w_{but}(\boldsymbol{x}) - w_{sub}(\boldsymbol{x}) - g_{cavity} = 0 \tag{4}$$

where $w_{sub}(\boldsymbol{x})$ is the downward directed displacement component of the flexible substrate top surface (which could result from the bending of the flexible substrate) and $w_{but}(\boldsymbol{x})$ represents the downward directed displacement component of the butterfly structure bottom surface, as depicted in Fig. 5b.

The contact problem is solved by means of the penalty method[90,91].

A 3D finite element discretization is obtained by means of quadratic 18 nodes wedge elements, as depicted in Fig. 5c, d. Accordingly with the adopted mixed formulation in the SINR FEM domain, a quadratic interpolation is used for the unknown displacement field $\boldsymbol{u}(\boldsymbol{x})$ and a liner interpolation is used for the unknown pressure parameter field $\pi(\boldsymbol{x})$. The total number of element results are equal to 21,336 and the total number of Degrees Of Freedom (DOFs) is equal to 185,556.

Sensor performance computation

To compute the sensor performance a set of solutions of the static contact problem are obtained. In particular, a sweep analysis on the surface load intensity is carried out, considering the human tactile range of perception[92,93], for the case of pure shear and pressure, taking into account the initial fabrication-induced residual stresses.

Therefore, the gap capacitance contribution C_{gap} to the capacitance of the each independent pixel capacitor is calculated by means of numerical integration through the expression (5)

$$C_{gap} = \int_{S_e} \frac{\varepsilon_{air}\varepsilon_0}{g_{cavity} + w_{sub}(\boldsymbol{x}) - w_{but}(\boldsymbol{x})}\, dA \tag{5}$$

where S_e is the overlapping electrode area between the top electrode and the corresponding bottom one, ε_{air} represents the air relative dielectric constant and ε_0 is the vacuum dielectric constant.

Considering the presence of the Si_3N_4 layer with thickness th_{s1}, as a separation between the Ti/Pt top electrode and the air gap, the expression (6) gives the Si_3N_4 related capacitance contribution $C_{Si_3N_4}$ of each independent pixel capacitor

$$C_{Si_3N_4} = \varepsilon_{Si_3N_4}\varepsilon_0 \frac{S_e}{th_{s1}} \tag{6}$$

in which, $\varepsilon_{Si_3N_4}$ is the Si_3N_4 relative dielectric constant.

Thus, the total capacitance C of each independent pixel capacitor is obtained by calculating the equivalent capacitance given by C_{gap} and $C_{Si_3N_4}$ connected in series, obtained through (7)

$$C = \frac{C_{gap}C_{Si_3N_4}}{C_{gap} + C_{Si_3N_4}}. \tag{7}$$

The sensor performance, in terms of variation of capacitance ΔC with respect to the initial one C_0, is expressed as

$$\Delta C = C - C_0 \tag{8}$$

where C_0 is the initial capacitance value which includes deformation induced by residual stress in the layers. C_0 is obtained by substituting C_{gap_0} into Eq. (7). And C_{gap_0} itself accounts for initial deflection, which is computed by substituting $w_{sub}(\boldsymbol{x})_0$ and $w_{but}(\boldsymbol{x})_0$ into expression (5) as initial displacement fields due to the fabrication-induced residual stresses.

By selecting $S_{e_{11}}$, namely S_e that corresponds to C_{11}, Eqs. (5) and (6) give, respectively, $C_{gap_{11}}$ and $C_{Si_3N_4 11}$; consequently, (7) and (8) give, respectively, C_{11} and ΔC_{11} corresponding to the total capacitance and variation of capacitance. The same rule applies to the capacitances of the other independent pixel capacitors C_{12}, C_{21} and C_{22}.

Analytical model

Analytical modeling of MEMS sensors and structures, which can be derived from relatively simplified formulation for kinematics and electrical capacitance, provides simple means to design and scale such devices. Although these idealized models have shortcomings in accurately accounting for initial deformation of structures and the behavior of the sensors in the post-contact regime, they still offer a useful understanding of how scaling may impact sensor performance.

In the analytical model, we assume that the layered system is flat.

For the case of an applied pressure, the change of the capacitance of the device is that of a parallel plate closing gap capacitor, thus Eq. (5) can be re-expressed with $w_{but}(\boldsymbol{x}) = w_{bump}$ where w_{bump} is the induced vertical displacement of the central bump. This scenario is reported in Fig. 5e.

However, the rigid vertical movement w_{bump} is not a representative kinematic quantity because of the established initial contact between the butterfly plate and the substrate, due to the fabrication-induced residual stresses, as reported in Fig. 6.

The proposed schematization is too simplistic. It purely provides the reader the ideal representation of the induced pressure sensing motion. Hence, the derived 3D FEM approach is used hereafter.

For the case of a pure shear force, if the small angle deflection is very reasonably assumed, i.e., $\sin\Theta \approx \Theta$, then the denominator in Eq. (5) can be written under the form $g_{cavity} - \Theta x$, where x is the horizontal coordinate along the length of the butterfly layered plate. The rotation angle of the structure Θ itself is obtained from the tilt geometry, as shown in Fig. 5f, which can be approximated as $\Theta \approx u_x/\mathrm{th}_{bump}$, where here u_x is the horizontal displacement of the bump under shear load, and th_{bump} is the thickness of the bump.

Two cases can be identified in a tilting displacement, the first case is where a capacitor's gap is reduced, while on the other side of the pivot point the capacitor's gap is increased. As such, the total capacitance change obtained by integrating Eq. (5) and inserting the obtained C_{gap} in Eqs. (7) and (8) is expressed, for the gap opening side, as

$$\Delta C = C_0 \frac{C_{Si_3N_4}}{(C_{gap_0}\kappa + C_{Si_3N_4})}(\kappa - 1) \tag{9}$$

where $\kappa = \frac{\log(1+\Theta L/g_{cavity})}{\Theta L/g_{cavity}}$ and for the gap closing side, as

$$\Delta C = -C_0 \frac{C_{Si_3N_4}}{(-C_{gap_0}\kappa + C_{Si_3N_4})}(\kappa + 1) \tag{10}$$

where $\kappa = \frac{\log(1-\Theta L/g_{cavity})}{\Theta L/g_{cavity}}$. Where L is the electrode's width.

Unlike the case of pressure force, a shear force will result in one capacitance decreasing while the opposite capacitance increases thus enabling a differential style readout between the two capacitors.

Numerical and experimental results

Mechanical response

The proposed 3D FEM model properly captures the initial deflection of the MEMS-based sensing structure due to the effect of the fabrication induced residual stresses. Figure 6a shows a picture of the embedded MEMS initial configuration taken with an optical microscope, where, the interference fringes indicate that the system is deformed.

In fact, the butterfly structure's four wings are bent upwards. While, the MEMS central part is deflected downwards. A limited area below the bump footprint is in contact with the substrate, as reported in Fig. 6b where negative displacements are observed.

The embedded MEMS surface topography is measured by means of an optical profilometer Lyncée Tec Digital Holographic Microscope (DHM). The corresponding numerically computed configuration is shown in Fig. 6c. The 3D model shows the upward concavity of the butterfly wings.

The numerical results show a perfect two-axis symmetrically deformed configuration. It is worth mentioning that, in the experimental data, it is only nearly two-axis symmetric because of the imperfections of the fabrication process, which is not included in the numerical model. However, FEM results largely confirm the effects of the in-plane fabrication-induced residual stresses.

The maximum measured upward displacement occurs at the butterfly tip corners. Considering the average over the four corners tips values, which is equal to 807 nm,

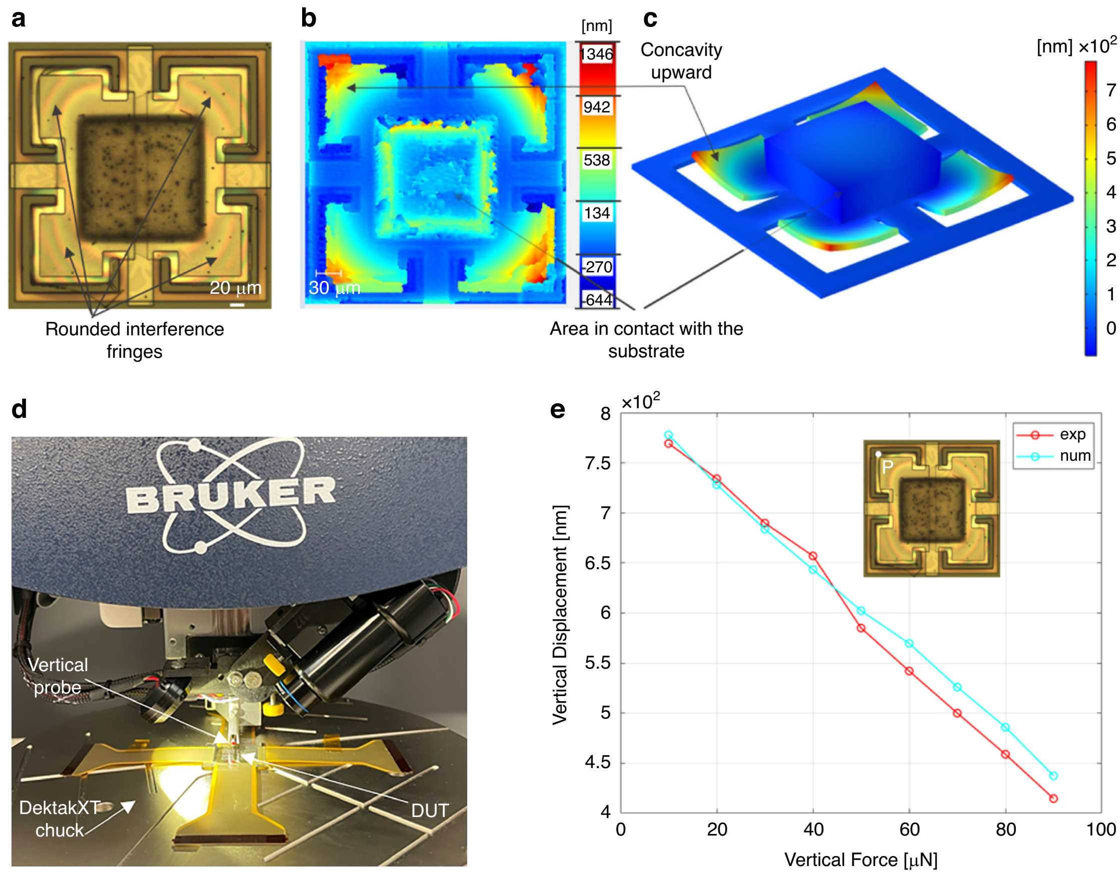

Fig. 6 Mechanical characterization of the embedded MEMS. a Initial configuration detected by the optical microscope with description of the rounded fringes of interference. **b** Measured initial topography by means of Lyncée Tec DHM. **c** Numerically computed vertical displacement. 3D plot over the initial deformed configuration with exaggerated deformation. **d** Vertical Force - Displacement pointwise load test: detail of the Device Under Testing (DUT) and the testing equipment. **e** Obtained Vertical Force - Displacement data: experimental curve in red, numerical curve in cyan. Top right inset of the force application point P at the butterfly wing tip

whereas the maximum numerical displacement occurs at the same location and is equal to 793 nm.

A mechanical pointwise load test is carried out to validate the described 3D FEM model under an external force condition. Figure 6d shows a detail of the Device Under Testing (DUT). In particular, a concentrated vertical force directed downward is applied to the corner tip of a butterfly wing where the maximum induced flexural response occurs.

The force point of application is indicated with P in the inset of Fig. 6e. The load varies linearly in the range [10–90 µN] and it is controlled by a load probe connected to the DektakXT stylus profilometer that detects the induced vertical displacement. Hence, a Force - Displacement experimental curve is obtained. The test condition is numerically replicated by means of the 3D FEM model. The measured and numerical data are presented in Fig. 6e. Here too, numerical and experimental results show an excellent agreement.

Electrostatic response

The electrostatic response of the embedded MEMS is measured by the Keysight E4980A Precision LCR Meter, in these measurements the capacitance dependence on voltage is quantified. Among the various single pixel capacitors, no variations are observed, hence it is representative of the average behavior, and we denote the voltage-dependent capacitance as C. The test is carried out by applying a linear static voltage ramp, in the range [0–8 V], to the embedded MEMS integrated top electrode while the bottom one is grounded. Note that no external mechanical load is simultaneously applied for this characterization. As a consequence of the linear voltage ramp, the embedded MEMS is subjected solely to electrostatically induced distributed forces. They bend the butterfly wings toward the substrate, closing the capacitor gap. The applied voltage and the data acquisition are controlled through a Python script running on a laptop. The test represents a preliminary check of the electrical

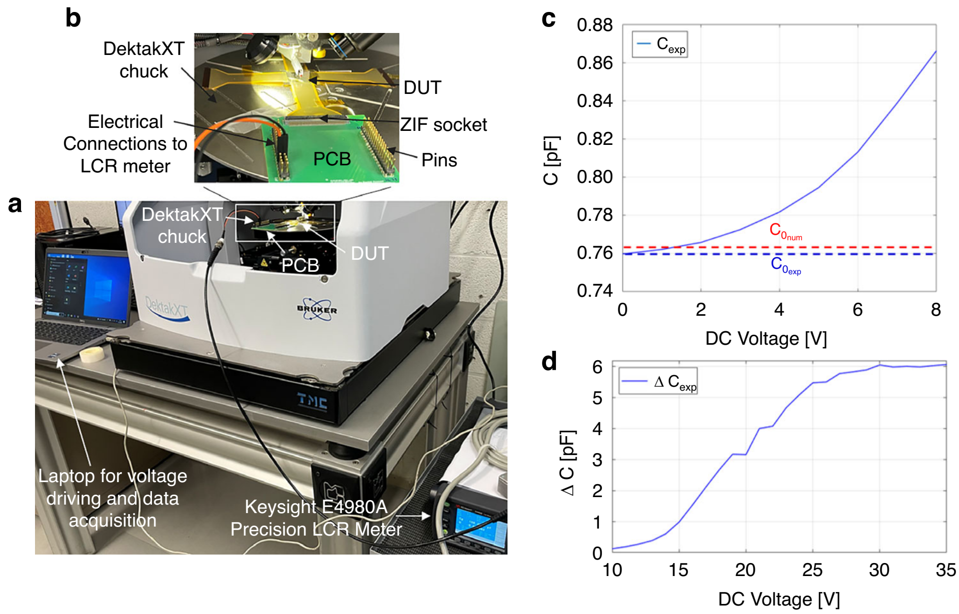

Fig. 7 Electrostatic characterization. a Experimental setup. **b** Detail of the DUT connected to the PCB on the DektakXT chuck. **c** Measured DC Voltage - Capacitance curve obtained by means of the Keysight E4980A Precision LCR Meter with reported measured C_0 in blue dashed line and numerical C_0 in red dashed line. **d** Electrostatic saturation test

and mechanical integrity of the sensing pixel before the pressure and shear characterization. Figure 7a shows the experimental setup. The DUT is mounted on the DektakXT chuck only for convenience, as presented in Fig. 7b. Note that the flexible connector is plugged in the dedicated Printed Circuit Board (PCB) through an electrical Zero Insertion Force (ZIF) socket with 68 independent channels each and every one connected to a single independent metallic pin on the sides of the PCB.

The DC Voltage - Capacitance curve is reported in Fig. 7c. The measured initial capacitance C_0 corresponds to no voltage applied, and it is only due to the initial separation and deflection of the MEMS butterfly structure. It is equal to 0.76 pF and indicated with a blue dashed line. The corresponding numerically simulated value of C_0 is indicated with a red dashed line. It is obtained by means of the 3D FEM model, by inserting the fabrication stresses induced pre-deformation fields $w_{sub}(\boldsymbol{x})_0$ and $w_{but}(\boldsymbol{x})_0$ into Eq. (5), and applying Eq. (7). It results in a C_0 value of 0.764 pF. Therefore, the numerical model correctly replicates the initial electrical capacitance. An electrostatic saturation test up to 35 V DC, carried out with the described set-up, shows a saturation capacitance variation of around 6 pF. It is obtained when the MEMS gap is fully closed because of the butterfly wings downward bending and the in parallel capacitance C reduces to $C_{Si_3N_4}$. The observed experimental trend, with the voltage increment is in line with the expected capacitive MEMS behavior of suspended movable plate capacitors where the capacitance increases as the function $y(x) = x^{-1}$ because of the gap reduction induced by the increasing applied voltage[94].

Pressure response

The experimental pressure characterization is carried out to measure the pixel response when a pressure is transmitted to the bump and detected by the capacitive sensing pixel. In particular, an external load is applied via the vertical load probe connected to the DektakXT, while the capacitance variation ΔC is detected by the Keysight E4980A Precision LCR Meter. A detailed picture of the DUT is taken by an optical microscope and shown in Fig. 8a where the vertical load probe tip shadow is highlighted together with the bump top surface, while the corresponding 3D FEM model load condition, where the load is superimposed on the pre-deformed device is shown in Fig. 8b. The diamond load probe tip has a radius of 25 μm. Applied vertical forces ranges from 30 μN up to 141 μN resulting in the reported pressure range by simply dividing the force value by the diamond tip contact area. Figure 8c shows the obtained measured and numerically computed results in terms of capacitance variation ΔC for each considered pressure intensity indicated with p. In particular, the symmetry of the design implies a symmetric mechanical response where each capacitance variation is equal and is indicated by ΔC. The capacitance changes replicated by the 3D FEM model fit with the measured experiments. The model is validated with

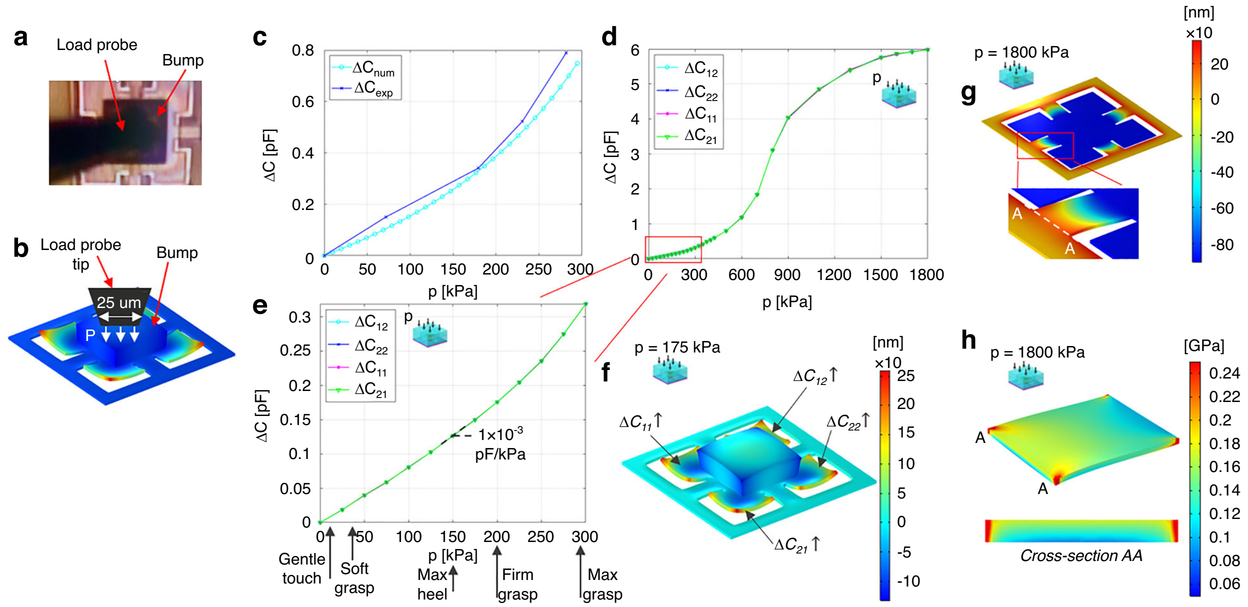

Fig. 8 Pressure characterization. **a** Optical microscope image of a detail of the DUT with highlighted vertical load probe shadow and bump surface. **b** 3D FEM model representative load condition. **c** Pressure - Capacitance Variation curves: measured in blue and numerically computed in cyan. **d** Numerically computed full-scale Pressure - Capacitance Variation curve. **e** Numerically computed Pressure - Capacitance Variation curve in the range of human skin pressure perception. **f** Numerically computed embedded MEMS vertical displacement induced by the combination of the residual stresses and $p = 175$ kPa. Highlighted capacitance increments. Plot depicted on the related deformed configuration with exaggerated motion. **g** Numerically computed embedded MEMS Si_3N_4 dielectric layer vertical displacement induced by the combination of the residual stresses and $p = 1800$ kPa. Plot depicted on the related deformed configuration with exaggerated motion. **h** Numerically computed longitudinal bridge stress induced by the combination of the residual stresses and $p = 1800$ kPa. Highlighted cross-section AA stress distribution

respect to the pressure load condition. The full-scale pixel pressure response is then computed by means of the validated 3D FEM model, considering the operating condition of an applied pressure on the pixel top surface, up to the saturation pressure level of 1800 kPa. Figure 8d reports the full-scale pixel pressure response. In the lower range [0–300 kPa] the sensitivity is computed and a detail of the curve is shown in Fig. 8e. The adopted lower pressure range is in line with the human skin perception[92]. This is also indicated on the horizontal axis by the correspondence between the pressure intensity and typical human activities that involve a touch event. Indeed, a benchmark of the technology concerning a human-like tactile sensing application is presented.

The pressure sensitivity S_p^{pix} of a single sensing micro pixel is expressed as the tangent of the Pressure - Capacitance Variation curve in Fig. 8c. A sensitivity of $S_p^{pix} = 1 \times 10^{-3}$ pF/kPa is obtained, for a pressure of $p = 150$ kPa, corresponding to the maximum pressure at the hill during the gate. Multiple metrics for expressing the sensitivity are reported in literature. The normalized sensor sensitivity is obtained by dividing the computed S_p^{pix} by the initial capacitance C_0. It results $S_p^{nor} = S_p^{pix}/C_0 = 0.0013\,\text{kPa}^{-1}$ and it represents a sensor intrinsic sensitivity metric. Dobrzynska et al. report in ref. [67], a flexible 3D force sensor on a PI substrate, where the obtained normalized pressure sensitivity is $6.6 \times 10^{-4}\,\text{kPa}^{-1}$, in the human pressure range of perception. In the paper[95], Lee et al. show a flexible polydimethylsiloxane (PDMS)-based capacitive -axial tactile array capable of measuring forces up to 131 kPa. They report a normalized pressure sensitivity value equal to $2.3 \times 10^{-4}\,\text{kPa}^{-1}$. While in the work[96], they obtain a value of around $10^{-4}\,\text{kPa}^{-1}$ with a working device in the 0–250 kPa pressure range. Surapaneni et al. present in ref. [97] a polymer-based pressure and shear capacitive sensor, operating up to 120 kPa of pressure, with a measured normalized pressure sensitivity of $4.4 \times 10^{-4}\,\text{kPa}^{-1}$. Alternatively, the pixel pressure sensitivity can be expressed respect to the vertical resulting force F, instead of the pressure and normalized with respect to the initial capacitance C_0. The presented technology gives $S_F^{nor} = S_p^{nor}/A_{pix} = 14.44\,\text{N}^{-1}$, where $A_{pix} = 300\,\mu\text{m}^2$ is the pixel top surface size where the pressure is distributed. In ref. [64], Yulu et al. report a flexible 3D capacitive force sensor with sensitivity much better then the other reported ones in literature. They obtain a value of $2.375\,\text{N}^{-1}$. Hence, the sensitivity values of the presented device are much higher than those reported for state-of-the-art capacitive triaxial force sensors.

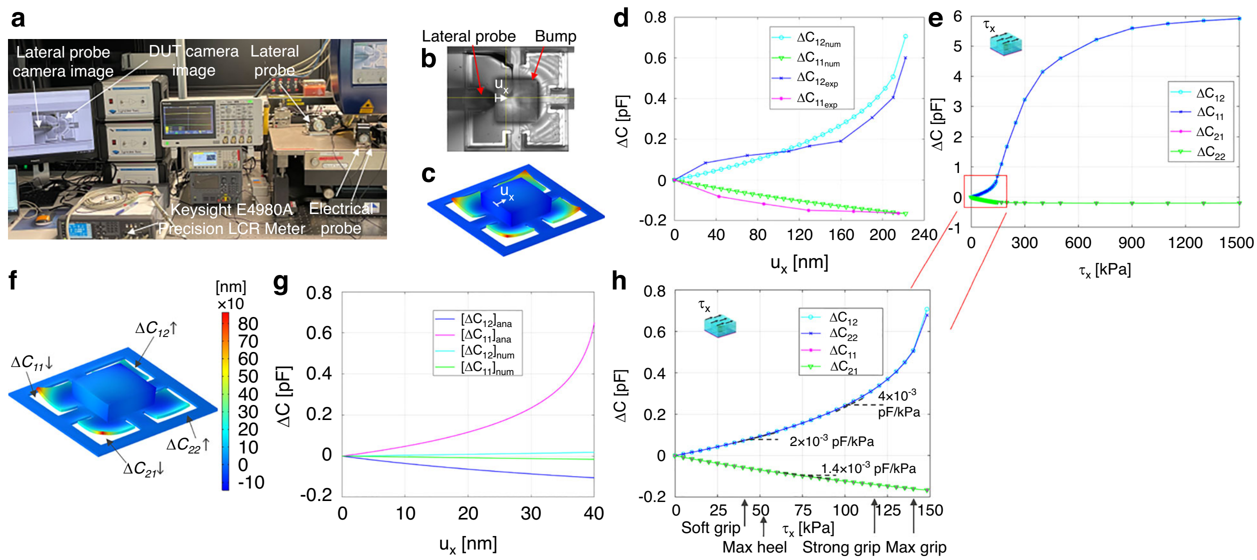

Fig. 9 Shear characterization. a Shear sensing mechanism characterization setup with highlighted DUT, lateral probe, electrical probes and Keysight E4980A Precision LCR Meter. **b** Optical microscope image of a detail of the DUT with highlighed lateral probe bump surface and applied displacement u_x. **c** 3D FEM numerical model representative load condition. **d** Lateral Displacement - Capacitance Variation curve: measured in blue and magenta, numerically computed in cyan and green. **e** Numerically computed full-scale Shear - Capacitance Variation curve. **f** Numerically computed embedded MEMS vertical displacement induced by the combination of the residual stresses and $u_x = 80$ nm, with highlighted capacitance variations. Plot depicted on the related deformed configuration with exaggerated motion. **g** Lateral Displacement - Capacitance Variation curve: analytical in blue and magenta, numerically computed in cyan and green. **h** Numerically computed Shear - Capacitance Variation curve in the range of human skin shear perception

Considering an applied pressure $p = 175$ kPa, the obtained numerical deformed configuration of the embedded MEMS sensing structure is shown in Fig. 8f. It is representative of the pressure sensing mechanism. Even if the bump is initially in contact with the substrate as an effect of internal stresses, it still deforms under the effect of the applied pressure, and the deformation of the bump is transmitted to the layered butterfly wings that consequently bend downward symmetrically with respect to the initial deformed configuration. These displacements induce the capacitor gap reductions and, therefore, the capacitance variations. The saturation pressure level of 1800 kPa gives a fully closed gap deformed configuration of the MEMS suspended plate, as reported in Fig. 8g where the Si_3N_4 dielectric layer surface is flat and moved down of a value equal to $g_{cavity} = 90$ nm, up to the substrate level. The maximum stress level coincides with the tensile longitudinal stress along the bridge axis. It is obtained at the bridge cross-section AA, in correspondence of the Si_3N_4 structural layer, and it is equal to 0.25 GPa, as shown in Fig. 8h. Note that it is far below the failure limit strength of CVD deposited Si_3N_4 thin film that results around 6 GPa, as reported in refs. [98,99]

Shear response

The experimental characterization of the shear sensing mechanism is carried out using the setup presented in Fig. 9a In this case, a controlled horizontal movement u_x is applied to the mid point of the bump top edge, by means of a lateral probe. The enforced displacement replicates the consequence of an applied horizontal shear load on the pixel top surface. The bump movement is recorded by the camera of the optical microscope. Hence, the displacement is obtained by the time frame recorded images. While the capacitance variations are measured by means of the Keysight E4980A Precision LCR Meter for each applied horizontal displacement intensity. The tests are replicated by means of the 3D FEM model.

Figure 9b reports the detail of the DUT picture taken by the camera of the optical microscope, in which the probe, the bump and u_x are highlighted. Figure 9c shows the corresponding representative 3D FEM model numerical load condition, where the horizontal displacement is superimposed on the initial configuration. While, Fig. 9d shows the obtained measured and numerically computed results in terms of capacitance variation ΔC, for each applied horizontal movement. The symmetry of the design implies an equal capacitance increase for the couple (C_{12}, C_{22}) and decrease for (C_{11}, C_{21}). Hence, only ΔC_{11} and ΔC_{12} are presented. The obtained numerical results show a good fit with the measured experimental ones.

The model is validated with respect to the shear sensing mode. The full-scale pixel shear response is then computed by means of the validated 3D FEM model, considering the operating condition of an applied shear on the pixel top surface, up to the saturation shear level of 1400 kPa. Figure 9e reports the full-scale pixel shear response. In the lower range [0–150 kPa] the sensitivity is computed and a detail of the curve is shown in Fig. 9h. Note that the maximum level of stress is here obtained in the case of $\tau_x = 1400$ kPa. It relates to the longitudinal tensile stress in the bridge. As the one presented in Fig. 8h, also in this case it is far below the limit strength.

Considering an applied horizontal displacement $u_x = 80$ nm the obtained numerical deformed configuration of the embedded MEMS sensing structure is shown in Fig. 9f. It is representative of the shear differential sensing mechanism. In particular, the bump movement is transmitted to the butterfly layered structure in which the wings defining the couple (C_{12}, C_{22}), placed on the side of the displacement verse, bends downward while the remaining other one, in correspondence of (C_{11}, C_{21}), bends upward. It results in an opposite change of capacitor gap that implies an increment of capacitance for the former couple and a decrement one for the latter.

The 3D FEM model Capacitance Variation - Lateral displacement curves are compared with the analytical ones obtained by means of the expressions (9) and (10). Figure 9g shows that the proposed analytical formulation abruptly overestimates the induced capacitance variations. As noted, the analytical model only considers the perfectly flat butterfly layered plate suspended over the four bridges, while the 3D FEM model includes the effect of the contact with the substrate that limits the induced butterfly movement. The results are reported up to $u_x = 40$ nm, since above this threshold the analytical formulation fails. In fact, the induced vertical movement of the butterfly's wings, that are closing that capacitor gap, exceed the initial gap g_{cavity}.

To compute the shear sensitivity, the 3D FEM numerical model is used to simulate a pure shear condition, oriented along the horizontal x direction, where the load is applied to the pixel top surface in combination with the fabrication-induced residual stresses, as described in Fig. 5a.

Hence, the corresponding capacitance variation of the four independent capacitors is computed for each analyzed value of the shear load intensity, in the range of human skin perception[93].

Figure 9h reports the numerical shear sensitivity S_τ^{pix} curves of the single pixel independent capacitors. It is worth noting that it results $S_\tau^{pix} = 2 \times 10^{-3}$ pF/kPa for the couple (C_{12}, C_{22}) in the case of τ_x around 40 kPa corresponding to a soft grip activated by grasping an object. While, it results $S_\tau^{pix} = 4 \times 10^{-3}$ pF/kPa considering $\tau_x = 100$ kPa associated with a good grip condition. Moreover, the couple (C_{11}, C_{21}) is characterized by an almost constant sensitivity $S_\tau^{pix} = -1.4 \times 10^{-3}$ pF/kPa in the analyzed range.

Considering τ_x around 40 kPa, the couple (C_{12}, C_{22}) normalized shear sensitivity is $S_\tau^{nor} = 2.6 \times 10^{-3}$ kPa^{-1} and the corresponding normalized shear force sensitivity results $S_H^{nor} = 28.88$ N^{-1}. Dobrzynska et al. report in ref. [67] an obtained normalized shear sensitivity of 2.8×10^{-4} kPa^{-1}, in the human pressure range of perception. In the paper[95], Lee et al. measure a value equal to 2×10^{-4} kPa^{-1}. While in the work[96], they obtain a value of around 10^{-4} kPa^{-1} with a working device in the 0–250 kPa pressure range. Surapaneni et al. present in ref. [97] a measured normalized shear sensitivity of 7.6×10^{-4} kPa^{-1}. In ref. [64], Yulu et al. report a normalized shear force sensitivity of 0.98 N^{-1} that is much better then the other reported ones in literature. Hence, the sensitivity values of the presented device are much higher than those reported for state-of-the-art capacitive triaxial force sensors.

Stability characterization

Since the structures presented in this work are based on traditional MEMS materials, e.g., silicon nitride and metals, they do not suffer from creep, fatigue, and plastic deformations as much as polymer-based touch sensors[39,100,101]. Therefore, we undertake dynamic cycling whereby the pixels are forced to vibrate at their resonance frequency with an amplitude of 4 nm, undergoing roughly 110 million cycles. The pixels show no change of resonance frequency, which would have indicated fatigue or stress relaxation, nor do they show change in the amplitude/voltage response, which would have indicated charging of the silicon nitride. This vibration amplitude corresponds to a displacement due to an applied pressure of 175 kPa, which corresponds to a firm grip, while the number of cycles would correspond to a usage over a full year, assuming a robotic manipulator operating at a rate of 1 grasp/second.

These measurements are carried out using a Polytec MSA-500 vibrometer. A structure pictured using the Polytec MSA-500 is shown in Fig. 10a. First, a frequency sweep is undertaken to determine the resonance frequency of the structure, Fig. 10b, then a continuous wave (CW) excitation is applied at the resonance frequency and the response of the structure monitored, Fig. 10c.

Array characterization

The array is primarily characterized in the electrostatics field. Figure 11a presents the DUT on the stage connected to Keysight E4980A Precision LCR Meter through an external PCB with a point probe to the Source Meter Unit (SMU) 2612B Keithley. The test is carried out using the described methodology in Section "Electrostatic Response" in which a linear static voltage ramp, in the

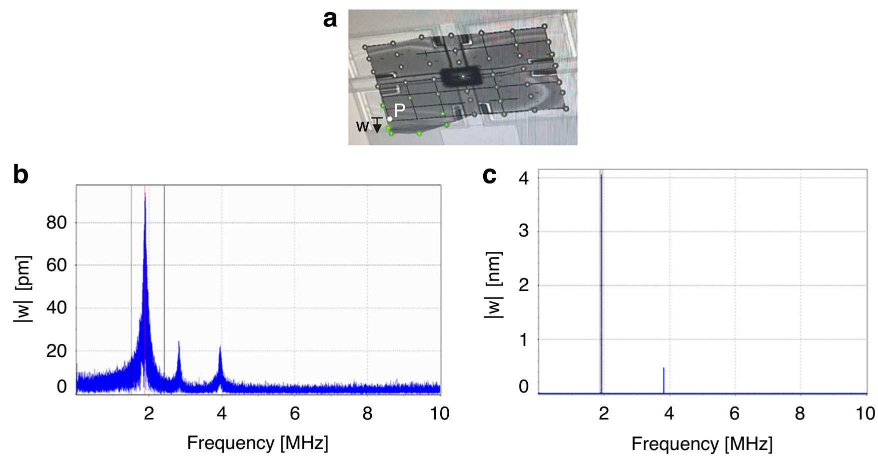

Fig. 10 Stability characterization. a Picture of the scan points defined in the Polytec MSA-500 to measure the vibrations of the structure. **b** Frequency sweep to determine the resonance frequency of the structure. **c** Continuous wave excitation at resonance, which results in a 4 nm displacement amplitude, is then monitored over the large cycling time

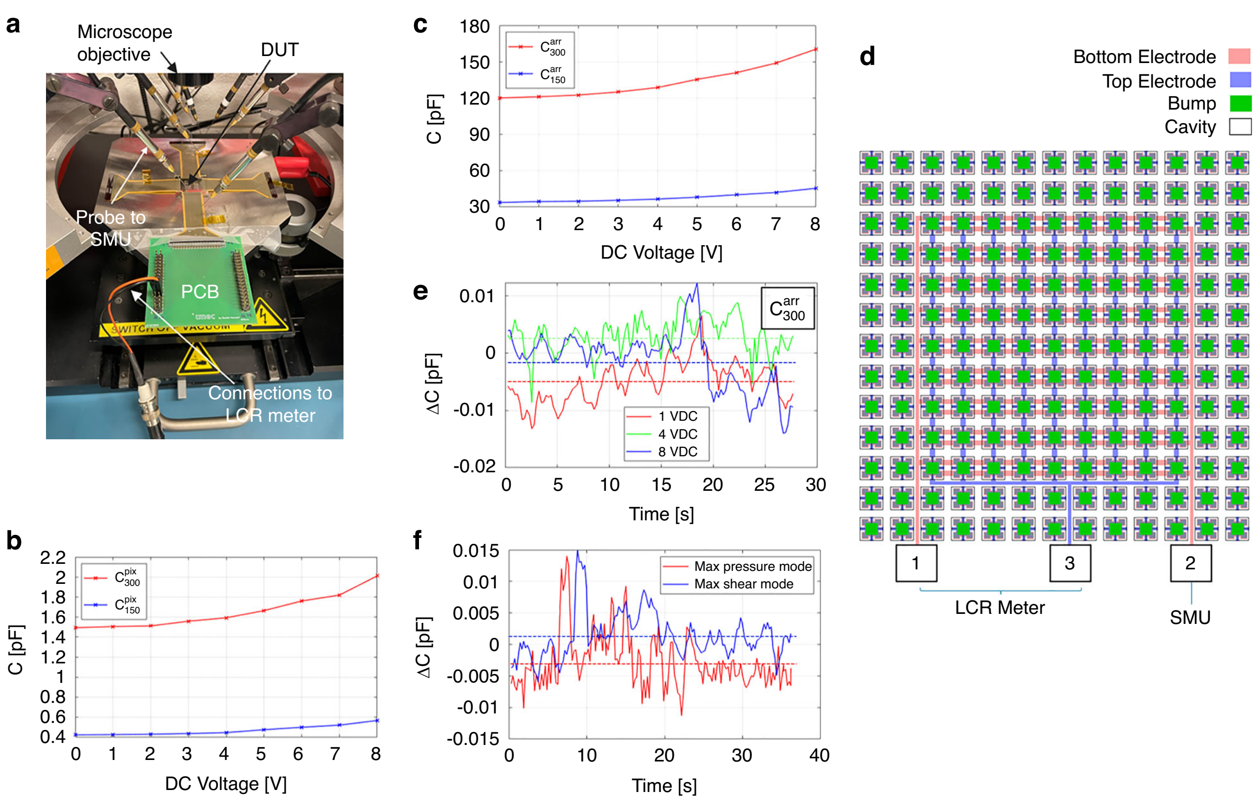

Fig. 11 Array characterization. a Experimental setup. **b** Single pixel measured DC Voltage - Capacitance curve. **c** Array measured DC Voltage - Capacitance curve. **d** Schematic representation of the crosstalk test. **e** Recorded crosstalk time signals with average values in dashed lines. **f** Recorded crosstalk time signals with average values in dashed lines for the max pressure and max shear modes

range [0–8 V], is applied to the embedded MEMS integrated top electrode while the bottom one is grounded. As a consequence, the MEMS is subjected solely to electrostatically induced distributed forces that bend the butterfly wings toward the substrate. Figure 11b shows the measured capacitance by means of the LCR Meter of an individual capacitor of a single pixel. The test is performed on two pixels, respectively, with 300 μm^2 and

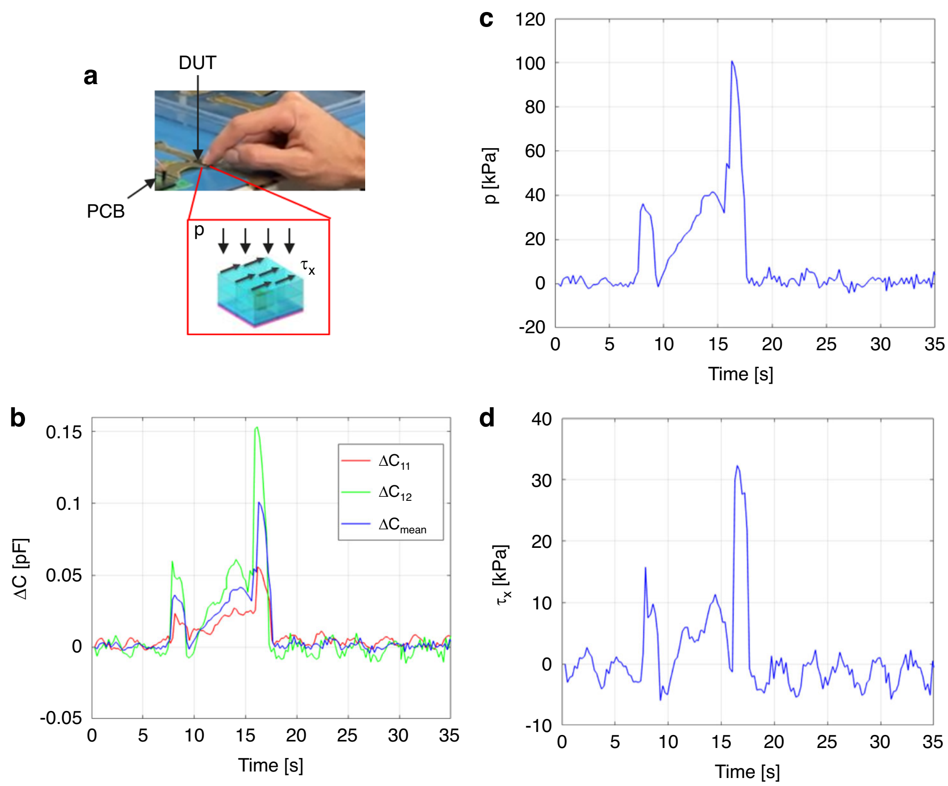

Fig. 12 Application validation. a Tactile stresses applied to an array under test. **b** Measured changes in capacitance due to the time-varying tactile stresses. Changes in capacitance are used to extract the pressure (**c**), and shear stresses (**d**), respectively

150 µm^2 size. The trend presented in Fig. 7c is here confirmed. The same test is performed on two 9 × 9 arrays where the measured pixels with 300 µm^2 and 150 µm^2 size are now connected in parallel with two independent channels, as illustrated in Fig. 11d. Note that the 9 × 9 array is surrounded by dummies, i.e., non-connected pixels. This mimics the large-array condition in which the considered 9 × 9 array is a sub-array of in-parallel-connected pixels. Figure 11c shows the measured single channel capacitance between top electrode, connected to the electric terminal 3, and bottom electrodes connected to the terminals 1 or 3. In this condition the SMU is not used. Such measurements can be performed using inline metrology, alongside the production line. The measured array capacitance scale up, with good approximation, with the total number of in-parallel-connected pixels in the array for different applied voltage and for both measured arrays. This represents a proof of a good pixel uniformity, i.e., response consistency. Note that, in the arrays, all the in-parallel-connected pixels are contemporary subjected to the same electrostatically induced distributed forces. Despite they are not due to an external mechanical load, they act as transmitted pressures distributed over the array of pixels. This test represents, additionally, a preliminary proof of the array responsiveness under distributed loads. To measure the crosstalk due to the applied electrostatic voltage, the SMU is connected to the pin 2, and a static voltage V DC is applied with values 1 V, 4 V and 8 V, while the induced capacitance variation is measured at the terminals 1–3 by means of the LCR meter. The time recorded signals are reported in Fig. 11e. Average values do not exceed 5 fF. Note that, this is not pure electrical crosstalk, instead, it represents a combination of electrical and mechanical one. It is due to the presence of both the input signal, i.e, the static voltage, and the induced electrostatic distributed forces. To solely measure the mechanically generated crosstalk, pressure and shear sensing mode tests are carried out over a single pixel. In this case, the methodology described in Section "Pressure Response" for the pressure case, and in Section "Shear response" for the shear one, is applied, while the crosstalk-induced variation of capacitance is measured over a neighbor-pixel under a zero-load condition, i.e. absence of applied pressure and shear stresses. For brevity's sake, the recorded time signals of the crosstalk-induced capacitance variations, over the load-free neighbor-pixel, are reported in Fig. 11f for the pure pressure case with maximum applied pressure, $p = 250$ kPa, and pure shear case with maximum shear-induced bump lateral displacement, $u_x = 200$ nm. They

are associated with the highest detected crosstalk level. The loaded pixel time recorded average values of the induced capacitance variations confirm the trend presented in the curves in Fig. 8c and Fig. 9d. In the case of the neighbor-pixel, under the load-free condition, the average recorded values of the crosstalk-induced capacitance variations do not exceed 3 fF. The result is justified by the fact that the pixels are physically separated, as illustrated in Fig. 2. It is a proof of the spatial independence, i.e. selectivity, of the sensing capability of the sensor array to correctly capture mechanical stimuli applied to only a certain restricted area, that in the lower limit coincides with the pixel footprint. This represents the hardest scenario for the selectivity evaluation, proving that an applied force distribution over the sensor patch can be mapped with a spatial resolution equal to the pixels inter-distance. The described experiments represent a preliminary array characterization that initially validates the adoption of the technology as a mechanical force sensor at the array level.

Array sensitivity

The advantage of a capacitive array-based sensor design consists in magnifying the signal by electrically collecting in parallel multiple pixels providing a potential scalability of the sensor patch sensitivity. Given the preliminary proved scalability of the array design, considering a $1\,\mathrm{cm}^2$ sensor patch, an array of 29×29 sensing pixels can be arranged and electrically connected in parallel in order to magnify the capacitance, of each independent capacitor, by a factor equal to the total number of in-parallel-connected pixels. Such an array would have an initial capacitance $C_0^{arr} = 640$ pF.

In realistic large-area robotics applications, during a touch event, applied forces may be considered resulting in pressure and shear uniformly distributed over $1\,\mathrm{cm}^2$ contact area with a reasonable approximation. As previously considered, the arrangement of 29×29 pixels, electrically connected in parallel, subjected to a distributed pressure $p = 150\,\mathrm{kPa}$, would have an array sensitivity $S_p^{arr} = 0.841\,\mathrm{pF/kPa}$.

Concerning the shear sensing, it leads to an array shear sensitivity for the couple (C_{12}, C_{22}) equal to $S_\tau^{arr} = 1.682\,\mathrm{pF/kPa}$ in correspondence of a soft grip and $S_\tau^{arr} = 3.364\,\mathrm{pF/kPa}$ for a good grip. Instead, the given array shear sensitivity for the couple (C_{11}, C_{21}) results $S_\tau^{arr} = -1.177\,\mathrm{pF/kPa}$. Furthermore, a combined differential sensitivity $S_{\tau,d}^{arr}$ can be assumed resulting in $S_{\tau,d}^{arr} = 2.859\,\mathrm{pF/kPa}$, considering the soft grip condition. Note that the reported array sensitivity values are predictions based on a preliminary array characterization and a pixel-level validated FEM model. Their accuracy will be assessed in dedicated future works by means of a deeper array characterization campaign.

Application validation

A validation of the usage of our fabricated devices as pressure and shear sensors is shown in Fig. 12a–d, where tactile stresses are applied to an array, as reported in Fig. 12a, and the induced changes in capacitance are measured and presented in Fig. 12b.

These changes in capacitance are, thereafter, used to extract pressure and shear stresses shown in Fig. 12c, d, respectively.

Conclusion

In this paper, a flexible capacitive MEMS-based triaxial force sensor is presented. The reported stack is compatible with the LA FPD cost-effective batch manufacturing. The design concept and the results of the fabrication are shown. The capacitive pixel response is investigated under the effect of the fabrication-induced residual stresses and the applied external pressure and shear load. A simplified analytical formulation is derived for sensing mechanisms. Considering the human skin range of pressure and shear perception, the device behavior is experimentally proved and correctly simulated by means of a 3D FEM model. In particular, the experimental and numerical results relate to: the initial deformed embedded MEMS configuration induced by the residual stresses; the pointwise vertical load-displacement mechanical behavior; the electrostatic capacitive response; the pressure and the shear sensing performance. Hence, the presented numerical model represents a valuable tool to provide a set of design guidelines for the sensor optimization.

The obtained pixel's normalized pressure sensitivity is equal to $0.0013\,\mathrm{kPa}^{-1}$. While the shear one results $2.6 \times 10^{-3}\,\mathrm{kPa}^{-1}$. The reported pixel's sensitivities are much higher than those reported for state-of-the-art capacitive triaxial force sensors. A preliminary experimental validation of the array sensing capability and scalability is given. Referring to a 29×29 array of pixels electrically connected in parallel, with $1\,\mathrm{cm}^2$ footprint, an initial capacitance equal to 640 pF of each independent capacitor element is estimated. The predicted pressure and shear sensitivities are 0.841 pF/kPa and 2.859 pF/kPa, respectively. An initial validation of the device performance is conducted at the array level through a human-finger touch test. Further array measurements will be performed, considering proper distributed mechanical load tests, and presented in dedicated future works.

Therefore, the presented technology represents a novelty and a solution for a highly sensitive LA flexible triaxial force sensor compatible with FPD batch manufacturing. It will open new frontiers in robotics and beyond by enabling multiple applications.

Acknowledgements
The authors would like to acknowledge Guilherme Brondani Torri for the helpful comments on the manuscript, Chloe Halbach and Clement Leruth for the precious discussion about the fabrication process.

Author contributions
G.M. conceptualized the device. G.M. and A.P. envisioned the process flow. G.M. developed the methodology, performed modeling and simulation, designed, fabricated the device and realized the results visualization. G.M. and S.H. carried out the experiments and investigations, wrote the original draft, reviewed and edited the manuscript. V.R. and J.G. supervised the work and provided the resources and the equipment for the simulation, design, fabrication and characterization.

Competing interests
The authors declare no competing interests.

Received: 26 February 2025 Revised: 1 December 2025 Accepted: 8 March 2026
Published online: 25 June 2026

References

1. Corzo, D., Tostado-Blázquez, G. & Baran, D. Flexible electronics: status, challenges and opportunities. *Front. Electron.* **1**, 594003 (2020).
2. Gharibans, A. A. et al. A novel scalable electrode array and system for non-invasively assessing gastric function using flexible electronics. *Neurogastroenterol. Motil.* **35**, e14418 (2023).
3. Liu, Y. et al. Highly flexible electronics from scalable vertical thin film transistors. *Nano Lett.* **14**, 1413–1418 (2014).
4. Zhang, Y. et al. Flexible electronics based on micro/nanostructured paper. *Adv. Mater.* **30**, 1801588 (2018).
5. Li, N. et al. Large-scale flexible and transparent electronics based on monolayer molybdenum disulfide field-effect transistors. *Nat. Electron.* **3**, 711–717 (2020).
6. Massimino, G., Rochus, V. & Genoe, J. Large area flexible triaxial force sensor array. In *2024 25th International Conference on Thermal, Mechanical and Multi-Physics Simulation and Experiments in Microelectronics and Microsystems (EuroSimE)*, 1–8 https://ieeexplore.ieee.org/abstract/document/10491428 (2024).
7. Ostyn, F., Vanderborght, B. & Crevecoeur, G. Series clutched actuation for collision-tolerant high-speed robots. *J. Mechanisms Robot.* **16**, 121008 (2024).
8. Elprama, S. A., Sander De Bock, R. M., Pauw, K. D., Vanderborght, B. & Jacobs, A. Design and implementation requirements for increased acceptance of occupational exoskeletons in an industrial context: a qualitative study. *Int. J. Hum. Comput. Interact.* **40**, 6051–6066 (2024).
9. Cao, H.-L. et al. Designing interaction interface for supportive human-robot collaboration: a co-creation study involving factory employees. *Comput. Ind. Eng.* **192**, 110208 (2024).
10. Agcayazi, T. et al. A scalable shear and normal force sensor for prosthetic sensing. In *2017 IEEE SENSORS*, 1–3 (IEEE, 2017).
11. Ostyn, F., Vanderborght, B. & Crevecoeur, G. Accelerating robotic picking of rigid objects with a compliant pneumatic gripper and an impact-aware trajectory plan. In *2024 IEEE International Conference on Robotics and Automation (ICRA)*, 1944–1949 (IEEE, 2024).
12. Scholz, C. et al. Improving robot-to-human communication using flexible display technology as a robotic-skin-interface: a co-design study. *Int. J. Intell. Robot. Appl.* **9**, 146–163 (2024).
13. Merckaert, K., Convens, B., Nicotra, M. M. & Vanderborght, B. Real-time constraint-based planning and control of robotic manipulators for safe human-robot collaboration. *Robot. Comput. Integr. Manuf.* **87**, 102711 (2024).
14. Nguyen, V.-C. et al. Haptic feedback device using 3d-printed flexible, multilayered piezoelectric coating for in-car touchscreen interface. *Micromachines* **14** https://www.mdpi.com/2072-666X/14/8/1553 (2023).
15. Massimino, G., Gazzola, C., Zega, V., Adorno, S. & Corigliano, A. Ultrasonic piezoelectric mems speakers for in-ear applications: Bubbles-like and pistons-like innovative designs. In *2022 23rd International Conference on Thermal, Mechanical and Multi-Physics Simulation and Experiments in Microelectronics and Microsystems (EuroSimE)*, 1–4 (|IEEE, 2022).
16. Massimino, G. et al. Air-coupled array of pmuts at 100 khz with pzt active layer: Multiphysics model and experiments. In *2019 20th International Conference on Thermal, Mechanical and Multi-Physics Simulation and Experiments in Microelectronics and Microsystems (EuroSimE)*, 1–5 (IEEE, 2019).
17. Yang, T.-H. et al. Recent advances and opportunities of active materials for haptic technologies in virtual and augmented reality. *Adv. Funct. Mater.* **31**, 2008831 (2021).
18. Robles-De-La-Torre, G. The importance of the sense of touch in virtual and real environments. *IEEE Multimed.* **13**, 24–30 (2006).
19. Grinberg, D. et al. 4d printing based piezoelectric composite for medical applications. *J. Polym. Sci. Part B* **57**, 109–115 (2019).
20. Massimino, G. et al. Multiphysics modelling and experimental validation of an air-coupled array of pmuts with residual stresses. *J. Micromech. Microeng.* **28**, 054005 (2018).
21. Massimino, G. et al. Multiphysics analysis and experimental validation of an air coupled piezoelectric micromachined ultrasonic transducer with residual stresses. *Procedia Eng.* **168**, 852–855 (2016).
22. Massimino, G., Colombo, A., Ardito, R., Quaglia, F. & Corigliano, A. Piezo-micro-ultrasound-transducers for air-coupled arrays: Modeling and experiments in the linear and non-linear regimes. *Extrem. Mech. Lett.* **40**, 100968 (2020).
23. Massimino, G., Ardito, R., Quaglia, F. & Corigliano, A. On the effects of package on the pmuts performances—multiphysics model and frequency analyses. *Micromachines* **11** https://www.mdpi.com/2072-666X/11/3/307 (2020).
24. Massimino, G., Quaglia, F., Corigliano, A. & Frangi, A. Model order reduction for the analysis of large arrays of piezoelectric micromachined ultrasonic transducers in water. *Appl. Acoust.* **182**, 108231 (2021).
25. Massimino, G., Lazarova, B., Quaglia, F. & Corigliano, A. Air-coupled pmuts array with residual stresses: experimental tests in the linear and non-linear dynamic regime. *Int. J. Smart Nano Mater.* **11**, 387–399 (2020).
26. Gazzola, C. et al. Mechanically-open and acoustically-closed PiezoMEMS Speakers: Innovative Designs for In-Ear Applications. In *16ème Congrès Français d'Acoustique, CFA2022* https://hal.science/hal-03848332 (Société Française d'Acoustique and Laboratoire de Mécanique et d'Acoustique, Marseille, France, 2022).
27. Massimino, G. *Modelling and simulation of piezoelectric micromachined ultrasonic transducers*. Ph.D. thesis, Politecnico di Milano https://www.politesi.polimi.it/handle/10589/166642 (2020).
28. Abdalla, O. M. O., Massimino, G., Savoia, A. S., Quaglia, F. & Corigliano, A. Efficient modeling and simulation of pmut arrays in various ambients. *Micromachines* **13** https://www.mdpi.com/2072-666X/13/6/962 (2022).
29. Abdalla, O. M. O. et al. Efficient modeling and simulation of large pmut arrays for biomedical applications. In *2025 26th International Conference on Thermal, Mechanical and Multi-Physics Simulation and Experiments in Microelectronics and Microsystems (EuroSimE)*, 1–5 (EuroSimE, 2025).
30. Abdalla, O. M. O., Massimino, G., Quaglia, F., Passoni, M. & Corigliano, A. Pmuts arrays for structural health monitoring of bolted-joints. *Micromachines* **14** https://www.mdpi.com/2072-666X/14/2/311 (2023).
31. Abdalla, O. M. O. et al. An experimental and numerical study of crosstalk effects in pmut arrays. *IEEE Sens. J.* **23**, 29029–29041 (2023).
32. Ardito, R., D'Alessandro, L., Massimino, G., Procopio, F. & Corigliano, A. Multiphysics analyses of the effect of package on the performances of PMUT transducers. In *Proceedings - Coupled Problems* https://re.public.polimi.it/handle/11311/1048371 (2017).
33. Abdalla, O. M. et al. Numerical simulation of crosstalk effects in pmut arrays. In *2023 24th International Conference on Thermal, Mechanical and Multi-Physics Simulation and Experiments in Microelectronics and Microsystems (EuroSimE)*, 1–5 (IEEE, 2023).
34. Halbach, C. et al. Fabrication and characterization of large-area flexible capacitive micromachined ultrasound transducers. In *2024 IEEE 37th International Conference on Micro Electro Mechanical Systems (MEMS)*, 943–946 (IEEE, 2024).
35. Halbach, C. et al. Analysis of collapse–snapback phenomena in capacitive micromachined ultrasound transducers. *Micromachines* **16**, 160 (2025).
36. Massimino, G. et al. Air-coupled pmut at 100 khz with pzt active layer and residual stresses: multiphysics model and experimental validation. In *2017 18th International Conference on Thermal, Mechanical and Multi-Physics Simulation and Experiments in Microelectronics and Microsystems (EuroSimE)*, 1–4 (IEEE, 2017).
37. Abdalla, O. M. O. et al. Crosstalk effects in pmut arrays. In *2023 22nd International Conference on Solid-State Sensors, Actuators and Microsystems (Transducers)*, 853–856, https://ieeexplore.ieee.org/abstract/document/10517049 (2023).

38. Georgitzikis, E. et al. Flexible alscn based pmut arrays for conformal and wearable ultrasound. In *2025 IEEE International Ultrasonics Symposium (IUS)*, 1–4 (IEEE, 2025).
39. Jeong, Y. et al. Fully flexible pmut based on polymer materials and stress compensation by adaptive frequency driving. *J. Microelectromechanical Syst.* **30**, 137–143 (2021).
40. Rochus, V. et al. Design of novel ultrasound transducers compatible with large-area electronics. In *2024 25th International Conference on Thermal, Mechanical and Multi-Physics Simulation and Experiments in Microelectronics and Microsystems (EuroSimE)*, 1–5 (IEEE, 2024).
41. Gijsenbergh, P., Billen, M., Wysocka, D., Cheyns, D. & Rochus, V. Ultrasound imaging in mid-air using phased polymer pmut array. In *2021 21st International Conference on Solid-State Sensors, Actuators and Microsystems (Transducers)*, 62–65 (IEEE, 2021).
42. Chen, J. et al. Recent progress in essential functions of soft electronic skin. *Adv. Funct. Mater.* **31**, 2104686 (2021).
43. Niu, H. et al. Perception-to-cognition tactile sensing based on artificial-intelligence-motivated human full-skin bionic electronic skin. *Adv. Mater.* **34**, 2202622 (2022).
44. Guo, Y. et al. Recent advances in carbon material-based multifunctional sensors and their applications in electronic skin systems. *Adv. Funct. Mater.* **31**, 2104288 (2021).
45. Cai, Y. et al. Mixed-dimensional mxene-hydrogel heterostructures for electronic skin sensors with ultrabroad working range. *Sci. Adv.* **6**, eabb5367 (2020).
46. Qu, J. et al. Recent progress in advanced tactile sensing technologies for soft grippers. *Adv. Funct. Mater.* **33**, 2306249 (2023).
47. Goh, G. L. et al. A 3d printing-enabled artificially innervated smart soft gripper with variable joint stiffness. *Adv. Mater. Technol.* **8**, 2301426 (2023).
48. Jain, S., Dontu, S., Teoh, J. E. M. & Alvarado, P. V. Y. A multimodal, reconfigurable workspace soft gripper for advanced grasping tasks. *Soft Robot.* **10**, 527–544 (2023).
49. Pierre Claver, U. & Zhao, G. Recent progress in flexible pressure sensors based electronic skin. *Adv. Eng. Mater.* **23**, 2001187 (2021).
50. Hou, C. et al. Borophene pressure sensing for electronic skin and human-machine interface. *Nano Energy* **97**, 107189 (2022).
51. Liu, C. et al. 3d printing technologies for flexible tactile sensors toward wearable electronics and electronic skin. *Polymers* **10**, 629 (2018).
52. Gerratt, A. P., Michaud, H. O. & Lacour, S. P. Elastomeric electronic skin for prosthetic tactile sensation. *Adv. Funct. Mater.* **25**, 2287–2295 (2015).
53. Luo, S., Meng, Q., Li, S. & Yu, H. Research of intent recognition in rehabilitation robots: a systematic review. *Disabil. Rehabilit.* **19**, 1307–1318 (2024).
54. Wang, D., Gu, X. & Yu, H. Sensors and algorithms for locomotion intention detection of lower limb exoskeletons. *Med. Eng. Phys.* **113**, 103960 (2023).
55. Su, D., Hu, Z., Wu, J., Shang, P. & Luo, Z. Review of adaptive control for stroke lower limb exoskeleton rehabilitation robot based on motion intention recognition. *Front. Neurorobot.* **17** https://www.frontiersin.org/journals/neurorobotics/articles/10.3389/fnbot.2023.1186175 (2023).
56. Asano, S. et al. 3-axis fully-integrated capacitive tactile sensor with flip-bonded cmos on ltcc interposer. *Sensors* **17** https://www.mdpi.com/1424-8220/17/11/2451 (2017).
57. Zhao, Y., Yang, W., Shan, Y., Bian, H. & Liu, M. Design and calibration experiment of a novel rigid-flexible hybrid parallel three-dimensional force sensor with deformability. *IEEE Sens. J.* **18**, 8247–8255 (2018).
58. Lee, J. et al. A micro-fabricated force sensor using an all thin film piezoelectric active sensor. *Sensors* **14**, 22199–22207 (2014).
59. Noh, Y. et al. Image-based optical miniaturized three-axis force sensor for cardiac catheterization. *IEEE Sens. J.* **16**, 7924–7932 (2016).
60. Lee, J.-H., Yeh, S.-K. & Fang, W. Vertically integrated double-bridge design for cmos-mems tri-axial piezo-resistive force sensor. In *2020 IEEE 33rd International Conference on Micro Electro Mechanical Systems (MEMS)*, 693–696 (IEEE, 2020).
61. Takahashi, H. et al. Mems 6-axis force sensor chip for spike pins in athletic sports shoes. *Sens. Actuators A: Phys.* **363**, 114702 (2023).
62. Lee, Y. R., Chung, J., Oh, Y. & Cha, Y. Flexible shear and normal force sensor using only one layer of polyvinylidene fluoride film. *Appl. Sci.* **9** https://www.mdpi.com/2076-3417/9/20/4339 (2019).
63. Cheng, X., Gong, Y., Liu, Y., Wu, Z. & Hu, X. Flexible tactile sensors for dynamic triaxial force measurement based on piezoelectric elastomer. *Smart Mater. Struct.* **29**, 075007 (2020).
64. Liu, Y. et al. A flexible capacitive 3d tactile sensor with cross-shaped capacitor plate pair and composite structure dielectric. *IEEE Sens. J.* **21**, 1378–1385 (2021).
65. Yao, S. et al. Fabrication and experimental validation of a sensitive and robust tactile sensing array with a micro-structured porous dielectric layer. *Micromachines* **13** https://www.mdpi.com/2072-666X/13/10/1724 (2022).
66. Dobrzynska, J. A. & Gijs, M. A. Flexible polyimide-based force sensor. *Sens. Actuators A Phys.* **173**, 127–135 (2012).
67. Dobrzynska, J. A. & Gijs, M. A. M. Polymer-based flexible capacitive sensor for three-axial force measurements. *J. Micromech. Microeng.* **23**, 015009 (2012).
68. Yao, T. et al. Highly sensitive capacitive flexible 3d-force tactile sensors for robotic grasping and manipulation. *J. Phys. D Appl. Phys.* **53**, 445109 (2020).
69. Fernandes, J., Chen, J. & Jiang, H. Three-axis capacitive sensor arrays for local and global shear force detection. *J. Microelectromechanical Syst.* **30**, 799–813 (2021).
70. Massimino, G., Alexey, P. & Veronique, R. A force sensing device and a method for manufacturing a force sensing device. US Patent App. 9/058,520 (2025).
71. De Roose, F. et al. A thin-film, a-igzo, 128b sram and lprom matrix with integrated periphery on flexible foil. *IEEE J. Solid State Circuits* **52**, 3095–3103 (2017).
72. Fortunato, G., Pecora, A. & Maiolo, L. Polysilicon thin-film transistors on polymer substrates. *Mater. Sci. Semiconductor Process.* **15**, 627–641 (2012).
73. Jeon, Y. E. et al. Capacitive sensor array for fingerprint recognition. In *2016 10th International Conference on Sensing Technology*, 1–4 (ICST, 2016).
74. Tiao, Y.-S., Sheu, M.-L., Wu, S.-M. & Yang, H.-M. A cmos readout circuit for ltps-tft capacitive fingerprint sensor. In *2005 IEEE Conference on Electron Devices and Solid-State Circuits*, 631–634 (IEEE, 2005).
75. Bardhan Roy, R., Farhanieh, O., Ergün, A. S. & Bozkurt, A. Fabrication of high-efficiency cmuts with reduced parasitics using embedded metallic layers. *IEEE Sens. J.* **17**, 4013–4020 (2017).
76. Chiu, P.-H., Chen, Z.-H., Chang, L., Lin, T.-T. & Huang, T.-H. P-140: high bandwidth glass-based capacitive micromachined ultrasound transducers (g-cmuts) for medical imaging application. In *SID Symposium Digest of Technical Papers*, 54, 1667–1669 (Wiley Online Library, 2023).
77. Berry, S. et al. A scalable fabrication process for liquid crystal-based uncooled thermal imagers. *J. Microelectromechanical Syst.* **25**, 479–488 (2016).
78. Sharma, J., Fernando, S. & Tan, W. M. Integration of aln with molybdenum electrodes and sacrificial amorphous silicon release using xef2. *J. Micromech. Microeng.* **24**, 035019 (2014).
79. Chan, E. K. et al. Continuous color reflective display fabricated in integrated mems-and-tft-on-glass process. *J. Microelectromechanical Syst.* **26**, 143–157 (2017).
80. Liu, L., guo Liu, W., Cao, N. & long Cai, C. Study on the performance of pecvd silicon nitride thin films. *Def. Technol.* **9**, 121–126 (2013).
81. Iliescu, C. et al. Residual stress in thin films pecvd depositions. *J. Optoelectron. Adv. Mater.* **13**, 387–394 (2011).
82. Flack, W. W., Nguyen, H.-A. & Capsuto, E. A novel photosensitive material for redistribution and stress buffer reduction on 300mm wafers. In *Advances in Resist Technology and Processing XXIII*, 6153, 1435–1446 (SPIE, 2006).
83. Raia, L., Rondelli, N., Bianchessi, M. & Carminati, M. Microfluidic structures for large-scale manufacture combining photo-patternable materials. *RSC Adv.* **6**, 59155–59159 (2016).
84. Roos, M. M., Winkler, A., Nilsen, M., Menzel, S. B. & Strehle, S. Towards green 3d-microfabrication of bio-mems devices using adex dry film photoresists. *Int. J. Precis. Eng. Manuf. Green. Technol.* **9**, 43–57 (2022).
85. Mulloni, V., Capuano, A., Adami, A., Quaranta, A. & Lorenzelli, L. A dry film technology for the manufacturing of 3-d multi-layered microstructures and buried channels for lab-on-chip. *Microsyst. Technol.* **25**, 3219–3233 (2019).
86. Agirregabiria, M. et al. Fabrication of su-8 multilayer microstructures based on successive cmos compatible adhesive bonding and releasing steps. *Lab Chip* **5**, 545–552 (2005).
87. Myny, K. The development of flexible integrated circuits based on thin-film transistors. *Nat. Electron.* **1**, 30–39 (2018).
88. Taylor, R. L., Pister, K. S. & Herrmann, L. R. On a variational theorem for incompressible and nearly-incompressible orthotropic elasticity. *Int. J. Solids Struct.* **4**, 875–883 (1968).
89. Shariff, M. An extension of herrmann's principle to nonlinear elasticity. *Appl. Math. Model.* **21**, 97–107 (1997).

90. Chouly, F. & Hild, P. On convergence of the penalty method for unilateral contact problems. *Appl. Numer. Math.* **65**, 27–40 (2013).
91. Zang, M., Gao, W. & Lei, Z. A contact algorithm for 3d discrete and finite element contact problems based on penalty function method. *Comput. Mech.* **48**, 541–550 (2011).
92. Dargahi, J. & Najarian, S. Human tactile perception as a standard for artificial tactile sensing—a review. *Int. J. Med. Robot. Comput. Assist. Surg.* **1**, 23–35 (2004).
93. Asaga, E., Takemura, K., Maeno, T., Ban, A. & Toriumi, M. Tactile evaluation based on human tactile perception mechanism. *Sens. Actuators A Phys.* **203**, 69–75 (2013).
94. Daeichin, M., Miles, R. N. & Towfighian, S. Large-stroke capacitive mems accelerometer without pull-in. *IEEE Sens. J.* **21**, 3097–3106 (2020).
95. Lee, H.-K., Chung, J., Chang, S.-I. & Yoon, E. Normal and shear force measurement using a flexible polymer tactile sensor with embedded multiple capacitors. *J. Microelectromechanical Syst.* **17**, 934–942 (2008).
96. Lee, H.-K., Chung, J., Chang, S.-I. & Yoon, E. Real-time measurement of the three-axis contact force distribution using a flexible capacitive polymer tactile sensor. *J. Micromech. Microeng.* **21**, 035010 (2011).
97. Surapaneni, R., Park, K., Suster, M., Young, D. & Mastrangelo, C. A highly sensitive flexible pressure and shear sensor array for measurement of ground reactions in pedestrian navigation. In *2011 16th International Solid-State Sensors, Actuators and Microsystems Conference*, 906–909 (IEEE, 2011).
98. Edwards, R., Coles, G. & Sharpe, W. Comparison of tensile and bulge tests for thin-film silicon nitride. *Exp. Mech.* **44**, 49–54 (2004).
99. Shafikov, A. et al. Strengthening ultrathin si3n4 membranes by compressive surface stress. *Sens. Actuators A: Phys.* **317**, 112456 (2021).
100. Woodford, D. A. Stress relaxation, creep recovery, and newtonian viscous flow in silicon nitride. *J. Am. Ceram. Soc.* **81**, 2327–2332 (1998).
101. Wereszczak, A. et al. Stress relaxation of silicon nitride at elevated temperatures. In *Proceedings of the 19th Annual Conference on Composites, Advanced Ceramics, Materials, and Structures—A: Ceramic Engineering and Science Proceedings*, 519–528 (Wiley Online Library, 1995).